Revised mantle viscosity profile based on global GPS uplift rates and glacial isostatic adjustment model ICE-6G_D(VM5a)

Yifei Chen[1], Wei Chen[1], Jim Ray[2*], and Jiancheng Li[1]

[1]Key Laboratory of Geospace Environment and Geodesy, School of Geodesy and Geomatics, Wuhan University, Wuhan 430079, China
[2]National Oceanic and Atmospheric Administration, Silver Spring, MD 20910, USA (retired)

Key Points:

- GPS-derived global GIA uplift datasets MIDAS-AO and MIDAS-AOHS are derived and presented
- Revised 1-D viscosity profiles VM5aR_AO1 and VM5aR_AO2 are derived based on the new crustal uplift rates

[*]Retired

Corresponding author: Wei Chen, wchen@sgg.whu.edu.cn

Abstract

Crustal motion observations from Global Positioning System (GPS) networks have not yet been fully exploited in previous studies on glacial isostatic adjustment (GIA) and mantle rheology structure. In this study, we have isolated GIA signals from vertical velocity observations at rigorously selected (over 2,000) GPS stations from the Nevada Geodetic Laboratory (NGL) by removing the effects of atmospheric and oceanic loading, as well as changes in the contemporary glaciers. We have also attempted to include hydrological and sea-level loading corrections based on the most updated model products, but found them still not accurate enough for GIA-related studies. Therefore, we recommend the GPS-derived global GIA uplift rate dataset MIDAS-AO without hydrological and sea-level loading corrections applied. Under the constraints of MIDAS-AO uplift rates, we refined the VM5a viscosity model and obtained two revised viscosity profiles, VM5aR_AO1 and VM5aR_AO2, that differ by an extra layer in the transition zone of the latter profile. With respect to VM5a, VM5aR_AO1 indicates a slight increase of viscosity within the upper mantle, while VM5aR_AO2 favors a softer upper part of the upper mantle and a stiffer transition zone. Maps of the variations of model-dataset misfits show that our new viscosity profiles commonly recover a better fit for sites located at the Scandinavian Peninsula and south of the Hudson Bay.

Plain Language Summary

The crust of the Earth got unloaded due to the melting of continental-scale ice sheets since the Last Glacial Maximum (LGM). Except for the almost instantaneous rise and fall of the crust, there are also slow changes in the Earth's surface due to the viscoelastic response of the Earth's mantle beneath the crust, which is known as glacial isostatic adjustment (GIA). The rise and fall of the Earth's surface caused by melted ice, as an aspect of GIA, is still happening today. Continuous measurements from the Global Positioning System (GPS) can monitor displacements of the Earth's surface, including GIA-induced ones. After removing all the non-GIA signals in GPS data, we got datasets of GIA-induced crustal displacements derived from global GPS data. On the other hand, the rates of GIA-induced crustal displacements are controlled by the viscosity-depth profile of the mantle, and thus the observed GIA-induced crustal displacements (the GPS datasets developed by this study) can be used to refine the mantle viscosity-depth profile. Our revised viscosity-depth profiles can reproduce surface displacements better fitting the GPS measurements from the Scandinavian Peninsula and south of the Hudson Bay.

1 Introduction

Rheology is a branch of physics that deals with the deformation and flow of matter, especially the non-Newtonian flow of liquids and the plastic flow of solids. For the case of Earth, rheology is the study of the viscoelastic behavior of the mantle, or the relationship between force (stress) and deformation (strain) of mantle materials under a set of loading and environmental conditions. While mantle rheology controls most of the geoprocesses with geological time scales, such as the style of mantle convection as well as glacial isostatic adjustment (GIA) and the nature of thermal evolution (Karato, 2010), the constraints available on mantle rheology are often rather loose, leading to significant uncertainty in mantle viscosity-depth profiles. Time-dependent crustal motion after the collapse of continental-scale ice sheets during the Last Glacial Maximum (LGM, ~ 21,000 years ago) is the most frequently used observation that provides some constraints on the viscosity of the mantle (Karato, 2010; S. D. King, 1995), which is also the topic of the current study.

Since the LGM, the melting of ice causes the redistribution of surface loads, resulting in the slow flow of materials in the Earth's mantle that leads to crustal motions and relative sea level change as well as variations in the Earth's rotation and gravity field. These responses, largely governed by the viscosity of the mantle, are collectively termed as GIA and are evident in the long-term observations of various ongoing processes such as relative sea level (RSL) changes, present-day crustal deformation rates monitored by Global Positioning System (GPS) observations that are not due to tectonic processes, and present-day changes in the gravity field seen by satellite missions and field campaigns (e.g., M. A. King et al., 2010; Whitehouse, 2018; Spada, 2017; Roy & Peltier, 2018; Davis et al., 1999; Spada & Melini, 2019; Melini & Spada, 2019; Caron & Ivins, 2020; Steffen et al., 2010). GIA also results in changes in the orientation of the Earth's rotation vector and length of day, which also provide constraints on the rheology of the mantle (e.g., Nakada et al., 2018; Lau et al., 2016).

A number of studies obtained diverse viscosity results based on regional GIA in different areas. In the British Isles, upper mantle viscosity is $4-6\times10^{20}$ Pa s and lower mantle viscosity is $\geq 3\times10^{22}$ (Bradley et al., 2011); in Antarctica, upper mantle viscosity lies in the range $0.8-2.0\times10^{21}$ Pa s (Whitehouse et al., 2012); in Fennoscandia, upper mantle viscosity is about $2-4\times10^{20}$ (Steffen et al., 2010); and in North America, upper mantle viscosity is estimated to be 5.1 $(3.5-7.5)\times10^{20}$ and lower mantle viscosity is estimated to be 1.3 $(0.8-2.8)\times10^{22}$ (Lambeck et al., 2017). These differences themselves imply lateral heterogeneity in the viscosity structure of the Earth, which is expected to exist based on the nature of the mantle convection process (Roy & Peltier, 2015). Nevertheless, it is recognized that typical viscosities for the upper and lower mantle lie in the ranges $10^{20}-10^{21}$ Pa s and $10^{21}-10^{23}$ Pa s, respectively (e.g., Bradley et al., 2011; Whitehouse et al., 2012; Steffen et al., 2010; Lambeck et al., 2017; Argus et al., 2014; Lau et al., 2016; Caron et al., 2017; Nakada et al., 2018).

The VM5a model was established aiming to provide a global 1D mantle viscosity profile (Peltier & Drummond, 2008). However, in this model, the thickness of the lithosphere, the viscosity of the upper mantle, the viscosity of the top 500 km of the lower mantle, and the viscosity of the middle and bottom of the lower mantle are constrained by RSL histories from the British Isles, RSL data from Fennoscandia and Laurentia, and the rate of change of Earth's oblateness ($\dot{J}_2$) and polar wander, respectively (Argus et al., 2014). Due to the lateral heterogeneity in the mantle viscosity structure as discussed above, the VM5a model, constrained by regional GIA signals at several areas, may not represent the average viscosities of the planet well, and thus further improvements are indicated.

While the RSL data are limited to coastal regions, GPS data can offer much better spatial coverage. The abundant 3D displacement data provided by dense GPS coverage all over the globe (especially in North America, Europe, and Scandinavia) may enable us to better model the GIA-induced deformations globally and thus improve the 1D mantle viscosity profile (Simon et al., 2021; Steffen & Wu, 2011; Bock & Melgar, 2016). Schumacher et al. (2018) developed a new global GPS dataset (in the ITRF2008 frame) for GIA-induced crustal uplift rates consisting of around 4000 GPS sites. However, there are notable discrepancies between this dataset and uplift rates as predicted by various GIA forward models (Zhou et al., 2020). To obtain a spherically symmetric model of mantle viscosity expected to provide a suitable background viscosity structure for the whole globe via the GPS method, some improvements seem to be needed to the work of Schumacher et al. (2018). We focus on two aspects here: derivation of the observed GPS uplift rates and elastic corrections applied to separate GIA signals from other geoprocesses-related signals.

The Nevada Geodetic Laboratory (NGL) routinely updates station velocities in a global geocentric reference frame at over 17,300 GPS sites all over the globe. These velocities are estimated robustly from observed position time series using the Median In-

terannual Difference Adjusted for Skewness (MIDAS) method, a median-based GPS station velocity estimator that is insensitive to outliers, seasonality, step functions (abrupt changes) arising from earthquakes or equipment changes, and statistical data variability (Blewitt et al., 2016). In recent years, NGL has updated its GPS data processing strategy so that the new NGL GPS data are provided in the IGS14 reference frame (the IGS realization of the ITRF2014), with multiple updated measurement models and corrections applied (including ocean tidal loading correction) but without nontidal atmospheric, oceanic and hydrological loading corrections (Blewitt et al., 2018; Sibois et al., 2014; Moyer, 2003; Kedar et al., 2003; Bar-Sever, 1996; Bassiri & Hajj, 1993). In addition, the NGL modeling of tropospheric delays is particularly notable and effective at retaining the full nontidal atmospheric load signal in the observed station coordinate time series (Martens et al., 2020). Therefore, the new NGL GPS processing results offer us ideal resources to extract GIA signals.

While M. A. King et al. (2010) argued that corrections for signals associated with the global water cycle, atmospheric effects, and local tectonics or sediment compaction must be applied to these geodetic data to invert for the mantle rheology, the hydrological correction is absent due to the fact that the representation of long-term trends is a common problem among hydrological model simulations (Döll et al., 2014). Yet recently, the Earth System Modelling group at Deutsches GeoForschungsZentrum (ESMGFZ) updated their model of hydrological mass loads (HYDL, version 1.3) based on water storage from the new Land Surface Discharge Model (LSDM, version 2) using new European Centre for Medium-Range Weather Forecast (ECMWF) operational forcing data. The new model is consistent with the release 06 (RL06) of the Gravity Recovery and Climate Experiment (GRACE) Atmosphere and Ocean De-Aliasing Level-1B (AOD1B) product and has an improved long-term consistency due to the introduction of a time-invariant reference orography in continental regions (Dobslaw et al., 2017). We are interested in the issue of how state-of-the-art hydrological model simulations will contribute to the estimation of the GIA signals from GPS observational data. In this study, we will present two GPS datasets: one with the HYDL correction and denoted as MIDAS-AOHS, while the other is without the HYDL correction and denoted as MIDAS-AO. These two variants of GPS GIA datasets will be assessed with the help of GIA model predictions and the GPS dataset from Schumacher et al. (2018). The resulting datasets will then be used to invert the viscosity-depth profiles. An additional viscosity structure in the transition zone is tentatively introduced in the revision of the viscosity-depth profiles to further investigate the viscosity structure features embedded in our datasets.

Our work is arranged as follows. The GIA models adopted in this study are provided in Section 2, then the GPS data and corrections for non-GIA trends are described in Section 3. Furthermore, the software and method are set out in Section 4. Results and discussions are presented in Section 5, and final conclusions are given in Section 6.

2 GIA Models

ICE-6G_D (VM5a) is one of the ICE-NG (VMX) series of GIA models developed at the University of Toronto, and consists of the ICE-6G glaciation history, the VM5a mantle viscosity model, and the associated present-day global crustal uplift rates (Argus et al., 2014; Peltier et al., 2015; Purcell et al., 2016; Peltier et al., 2018, available at `https://www.atmosp.physics.utoronto.ca/~peltier/data.php`).

Reconstructed based on the BEDMAP2 bathymetry model, the ICE-6G model describes ice thickness histories of the major ice sheets from 122,000 years ago to the present and differs from previous ICE-NG models in that glaciation history has been explicitly refined by applying the present-day uplift rates estimated from GPS measurements from North America, Eurasia, and Antarctica. Besides, time-dependent gravity data derived from the GRACE satellites, and radiocarbon-dated relative sea level histories through

the Holocene epoch have also constrained or validated glaciation history (Peltier et al., 2018).

The viscosity model VM5a describes the rheological structure of the Earth's mantle (Peltier & Drummond, 2008, see Table 1). It is a 3-layer approximation of the viscosity model VM2, which is inferred on the basis of a formal Bayesian inversion of a subset of the RSL data that depend only weakly on the glaciation history and Earth rotation constraints (Peltier, 2004). For the VM2 model, the RSL histories from sites in Fennoscandia constrain the mean viscosity of the upper mantle and transition zone to be $\approx 0.5\times 10^{21}$ Pa s, while the RSL histories from sites in Laurentia constrain the mean viscosity of the upper 500 km of the lower mantle to be $\approx 1.6\times10^{21}$ Pa s; the wander of Earth's spin axis since 1900 and the non-tidal acceleration of Earth's rotation rate constrain the viscosity of the remainder of the mantle to be $\approx 3.2\times10^{21}$ Pa s (Argus & Peltier, 2010). The VM5a model also shares these properties but differs from VM2 in the structure of the lithosphere: while the VM2 lithosphere is entirely elastic and 90 km thick (Peltier, 2004), the VM5a lithosphere consists of a 60-km-thick elastic layer above a 40-km-thick highly viscous (10×10^{21} Pa s) layer. This additional layer introduced by VM5a can eliminate VM2's misfits of horizontal motion in the region of the North American continent and has no significant effect on the predicted rates of vertical motion and the quality of the fits to radio-carbon dated relative sea level histories from sites along the east coast of the US (Peltier & Drummond, 2008).

Table 1. Viscosity profile of VM5a.

Depth Range (km)		Viscosity ($\times10^{21}$Pa s)
0-60	(lithosphere)	elastic
60-100	(lithosphere)	10.0
100-420	(upper mantle)	0.50
420-670	(transition zone)	0.50[a]
670-1260	(lower mantle)	1.57
1260-2885.5[b]	(lower mantle)	3.23

[a]Transition zone shares the same value of viscosity with the upper mantle.
[b]In our computations this value is replaced by 2880.

In this study, we adopt the following forward models of GIA-induced crustal uplift rates to establish and test our global GPS-derived GIA uplift rate datasets:

1. ICE6G_D (VM5a) published by Peltier et al. (2018);
2. ICE6G_ANU_D published by Purcell et al. (2018);
3. Predictions published by Caron and Ivins (2020) (denoted as VESL 2019 for convenience).

3 GPS Data and Corrections

3.1 MIDAS velocity data

In this study, we have adopted the GPS-based vertical velocity data derived from the MIDAS algorithm (hereafter MIDAS velocity data for short; available at `http://geodesy.unr.edu/velocities/midas.IGS14.txt`, last accessed on 25 Nov. 2021). These data are derived from GPS position time series generated by the NGL at the University of Nevada, Reno (UNR). Before applying the MIDAS algorithm, the GPS data have been processed using the GPS Inferred Positioning System (GIPSY) OASIS II software by the

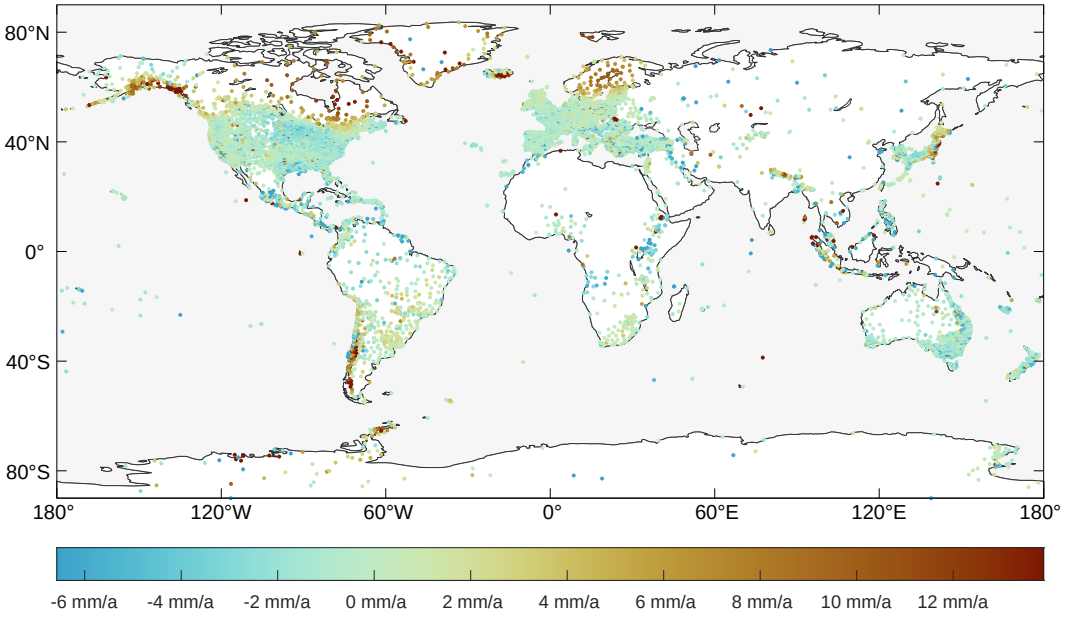

Figure 1. Distributions of the GPS sites of MIDAS velocity files. The colors of dots denote crustal uplift rates.

Jet Propulsion Laboratory (JPL) and using their final fiducial-free GPS orbit products. The precise point positioning method has been applied to ionospheric-free carrier phase and pseudorange data. More details about models and conventions used in the processing are documented at `http://geodesy.unr.edu`.

The MIDAS algorithm is a variant of the Theil-Sen nonparametric median trend estimator, modified to use pairs of data in the time series separated by approximately 1 year, making it insensitive to seasonal variation and time series outliers. And since the MIDAS-estimated velocity is essentially the median of the distribution of these 1-year slopes, it is insensitive to the effects of steps in the time series (even if they are undocumented and occur at unknown epochs) as long as they are sufficiently infrequent. The MIDAS uncertainties are calculated by using the scaled median of absolute deviations of the residual dispersion, and have been shown to be realistic and usually do not require further scaling. The MIDAS algorithm is reported to outperform all 20 other automatic algorithms tested in terms of the 5-th percentile range of accuracy in blind tests using synthetic data with unknown step functions inserted (Blewitt et al., 2016). Therefore, the MIDAS velocities are as accurate as the best methods involving step detection. These are the reasons why we have chosen the robust and unbiased estimations of MIDAS velocity data to establish the global GIA uplift rate dataset and invert the mantle viscosity profile.

The MIDAS velocity data contain estimated velocities of the north, east, and up components with corresponding uncertainties from more than 17,300 GPS sites (see Figure 1 for the site distributions over the globe) time series in the IGS14 reference framework, whose origin is the center of figure (CF; Blewitt et al., 2018; Altamimi et al., 2016). Only the vertical velocity data (up components of velocities) are adopted in this study.

First of all, GPS time series have to be sufficiently long for the purpose of the GIA study. Following Schumacher et al. (2018), GPS sites with data time spans less than 5 years are excluded.

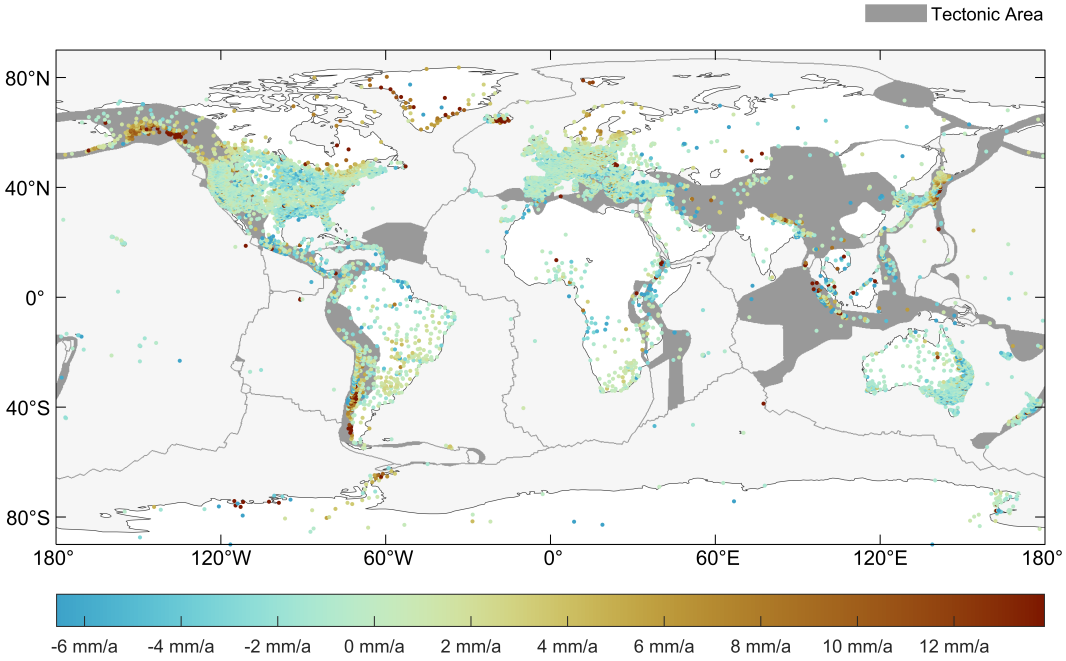

Figure 2. Stations that are excluded from the dataset for GIA purposes. Gray shading denotes plate boundaries and the colors of dots denote observed crustal uplift rates.

Second, a number of GPS sites are located near plate boundaries in order to study crustal displacements due to tectonics and earthquakes. For these sites, the GPS data are highly affected by tectonics and earthquakes and thus unsuitable for GIA-related studies. We can exclude the sites within the plate boundary zones relying on the Global Strain Rate Map released by Kreemer et al. (2014).

Finally, the prior information from global GIA forward model predictions ICE6G_D (VM5a) uplift rates (released by Peltier et al. (2018)) is adopted to ensure that only stations with vertical land motion (VLM) signals dominated by GIA are included. Considering the difference between GPS-derived uplift rates and modeled GIA rates to be non-GIA VLM signals, we can calculate the ratio $\dot{R}_{\mathrm{non-GIA}}/\dot{R}_{\mathrm{GIA}}$ at each site, and regard it as GIA dominant if $\dot{R}_{\mathrm{non-GIA}}/\dot{R}_{\mathrm{GIA}} < 0.5$ (Simon & Riva, 2020).

After three rounds of selection, we obtained 2,353 GIA-dominant sites, while about 15,000 sites are excluded. The distribution of excluded NGL GPS stations is shown in Figure 2 where plate boundaries are marked with gray color.

3.2 Elastic correction

To remove the elastic signal from GPS rates, we adopt general circulation model (GCM)-based elastic surface loading products provided by the ESMGFZ Section 1.3 (Dill & Dobslaw, 2013), involving 3 kinds of individual mass loading data: non-tidal atmospheric loading (NTAL), non-tidal oceanic loading (NTOL), and HYDL. And ESMGFZ additionally provides a special barystatic sea-level loading (SLEL) for the conservation of global mass. These non-tidal elastic surface loading deformations are calculated in the spatial domain by convolving the load Green's function for the elastic earth model "ak135" (Kennett et al., 1995) and are provided in the form of grid data with $0.5° \times 0.5°$ spatial resolution (available at `http://rz-vm115.gfz-potsdam.de:8080/repository`). ES-

MGFZ offers these elastic surface loading products both in the CF and CM frames. In this study, we have adopted those products in the CF frames.

NTAL is derived from the 3-hour sampled atmospheric surface pressure given by $0.5^\circ \times 0.5^\circ$ 3-hourly ECMWF reanalysis, ERA-40, ERA-Interim, and operational ECMWF data. To isolate the non-tidal variability of the atmosphere, atmospheric tides were removed by harmonic analysis of 12 major tidal constituents: main solar tides S1, S2, and S3, and the main semi-diurnal lunar tide M2, each with two additional side-bands added. Non-tidal atmospheric surface pressure is resampled on a regular $0.125^\circ \times 0.125^\circ$ global grid.

NTOL is derived from 3-hour sampled non-tidal ocean bottom pressure given on a regular $1.0^\circ \times 1.0^\circ$ global grid from the Max-Planck-Institute for Meteorology Ocean Model (MPIOM; Jungclaus et al., 2013) and consistent deformation fields from daily means of the ECMWF atmospheric surface pressure. Oceanic tides excited by the time-varying atmospheric surface pressure were removed by harmonic analysis of 12 major tidal constituents similarly as in NTAL. Non-tidal ocean bottom pressure is resampled on a regular $0.125^\circ \times 0.125^\circ$ global grid.

HYDL version v1.3 is based on water storage from new version-2 LSDM (Dill, 2008, updated glacier definitions in the Himalaya region) using new 24-hour $0.5^\circ \times 0.5^\circ$ ECMWF operational forcing data that was preprocessed to a commonly defined high-resolution reference topography in order to avoid inconsistencies between different ECMWF model setups (ERA-40, REA-Interim, operational). Mass loads are given from the LSDM as soil moisture, snow, surface water, and water in rivers and lakes on a daily regular $0.5^\circ \times 0.5^\circ$ global grid with mean mass during 2003˜2014 subtracted and are resampled to $0.125^\circ \times 0.125^\circ$ with a $0.125^\circ \times 0.125^\circ$ land-sea mask applied. Water stored in rivers and lakes is re-allocated from the model 0.5° river network to a high-resolution 0.125° geographic information system (GIS)-based river network (Dill et al., 2018) to concentrate the river masses to a more realistic river location than in the 0.5° model river network.

As atmospheric models, oceanic models, and hydrological models together generally do not conserve their global mass, especially most oceanic models only keep their own mass constant and do not consider the mass exchange with atmosphere and land, ESMGFZ introduced SLEL by solving the sea-level equation for the total mass of terrestrial water storage and atmospheric surface pressure to obtain global mass conservation (Dill & Dobslaw, 2019). SLEL is not included in the oceanic contribution NTOL. Therefore, the sum of the above four components (NTAL + NTOL + HYDL + SLEL) represents the complete surface loading deformation of a globally mass-conserving model system.

First, we extract the station time series of the complete elastic surface loading deformations by these stations' longitudes and latitudes from the gridded values. Second, we cut these time series off according to the MIDAS time series' first and last epochs. The resulting tendencies estimated from these time series are the ESMGFZ elastic corrections applied in this study (see Figure 3 for more details about ESMGFZ elastic corrections and see Figure S1 for more details about individual components of the ESMGFZ elastic corrections).

A seasonal-driven annual discharge model has been included in the LSDM model to accumulate and remove the annual snowfall, while long-term ice masses are kept constant (Dill, 2008). Nevertheless, the contemporary ice mass loading impact on elastic deformation is not included in the LSDM model. To remedy this, we compute present-day mass trend (PDMT) corrections at the NGL GPS sites, based on the grids released by Riva et al. (2017) spanning 2005-2014 (for the selection of this spanning, we referred to (Schumacher et al., 2018), and see Figure 4 for more details). Total elastic corrections

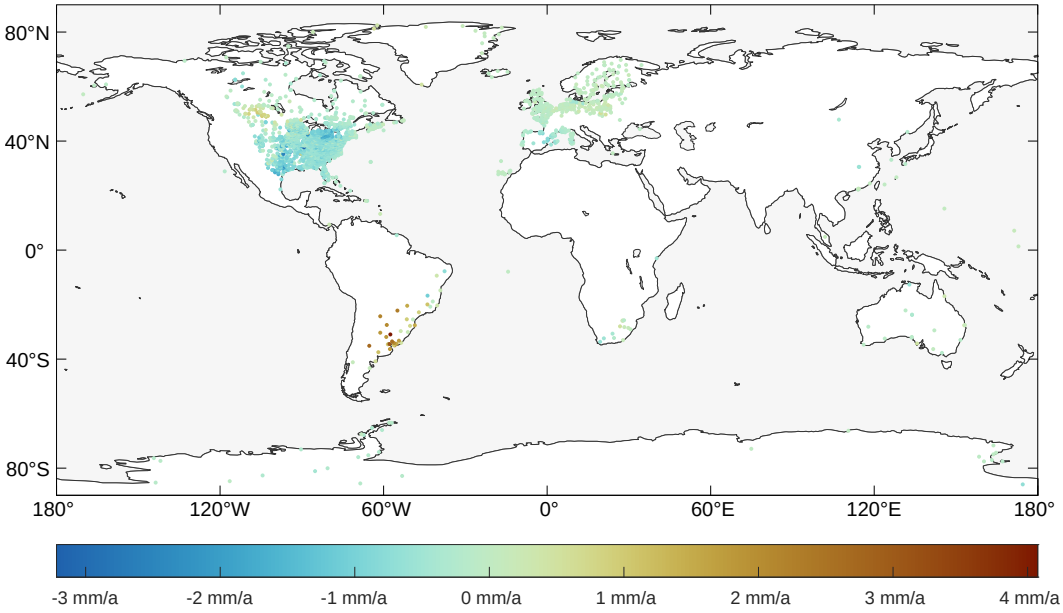

Figure 3. ESMGFZ elastic corrections (NTAL + NTOL + HYDL + SLEL) applied for GPS sites. The colors of dots denote crustal uplift rates.

(NTAL + NTOL + HYDL + SLEL + PDMT) applied for NGL GPS sites are illustrated by Figure 5.

Although Klos et al. (2021) suggests applying HYDL at the stage of time series analysis could reduce amplitudes in the seasonal and longer terms, some studies show that subtracting the hydrological loading by removing simulations from global hydrological models might introduce even more uncertainties, as surface hydrology is not well modeled in most models (Döll et al., 2014; Santamaría-Gómez & Mémin, 2015). Moreover, we note that HYDL is the most relevant one in the total environmental load (NTAL + NTOL + HYDL + SLEL) for long-term trends (see Fig S1 for more details). We ought to be more cautious about the application of HYDL (and SLEL) corrections. Therefore, we decided to present two parallel GPS datasets for GIA: one with NTAL + NTOL + HYDL + SLEL + PDMT corrections applied, denoted as MIDAS-AOHS, and one only with NTAL + NTOL + PDMT corrections applied, denoted as MIDAS-AO.

We notice that there are some outliers in our processed datasets after applying elastic corrections, which are very similar to the sharp "spikes" as shown in Figure 3 of Zhou et al. (2020). We infer that these outliers are caused by some local, not well-modeled effects, such as deep groundwater variations. Besides, sites affected by earthquakes outside the plate boundary zones may also be outliers.

We adopted a low-pass spatial filtering approach to exclude these outliers. For this, we applied a median filter with a $1.5^\circ \times 1.5^\circ$ moving window, consistent with the spatial resolution of the glaciation history and the precision of the forward modeling code. The absolute difference between the median value and the original value is taken as a selection criterion. Sites with this metric exceeding 3σ of the moving window scatter will be excluded.

Since the GIA forward model predictions are often provided in a reference frame with the origin in their own realization of the center of mass of the solid Earth (CE), while the MIDAS velocities are provided in a CF frame, we transformed our datasets into a CE frame by a pragmatic method to better assess the misfits between the GIA model

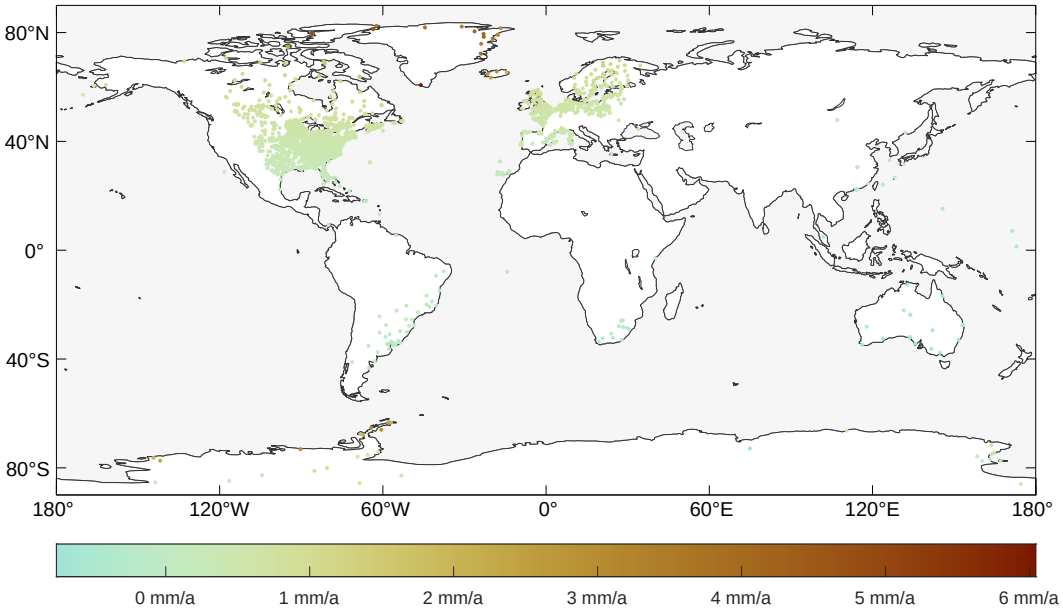

Figure 4. PDMT elastic corrections applied for GPS sites. The colors of dots denote crustal uplift rates.

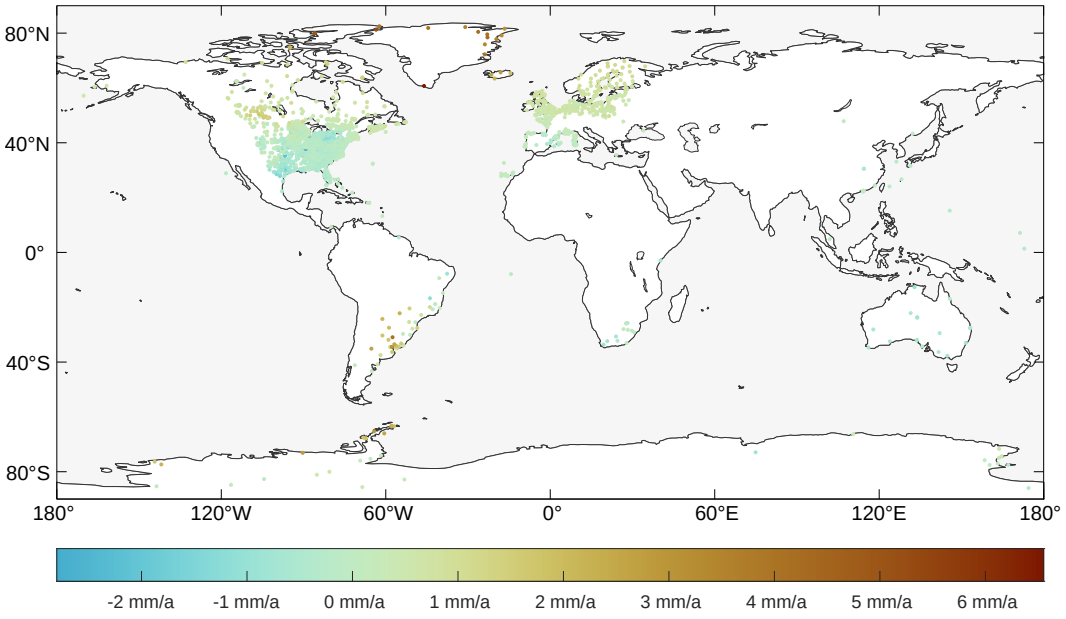

Figure 5. Total elastic corrections (NTAL + NTOL + HYDL + SLEL + PDMT) applied for GPS sites. The colors of dots denote crustal uplift rates.

predictions and our GPS-derived GIA datasets (M. A. King et al., 2012; Peltier et al., 2015; Schumacher et al., 2018). Finally, our GPS-derived GIA crustal uplift rates datasets MIDAS-AOHS and MIDAS-AO are presented here.

4 Software and Method

4.1 GIA Software

Based on the viscoelastic normal mode (VNM) theory, Spada (2003b) developed a Fortran-based posT glAcial reBOund calculatOr (TABOO), which can solve various problems in the context of GIA modeling, including crustal uplift rates due to loads of various shapes and time-histories. The TABOO software treats the Earth as a spherically symmetric, non-rotating, incompressible, self-gravitating, radially stratified Maxwell-viscoelastic body with an elastic lithosphere and a homogeneous, inviscid core (the inner core is not included), with profiles of elasticity and density from the preliminary reference Earth model (PREM) (Dziewonski & Anderson, 1981) but somewhat simplified. A benchmark for GIA codes by Spada et al. (2011) shows that computations implemented by TABOO have a satisfactory agreement with those implemented by other GIA codes, even with those based on different methods and solution techniques, like spectral-finite elements and finite elements.

While TABOO does not take account of effects of the Earth's rotation, the GIA-induced deformation will perturb the Earth's rotation at long-term scales (such as the polar wander), and as feedback, the changed rotation vector will lead to changes in centrifugal potential and thus additional crustal deformation (known as rotational feedback). However, only the degree-0 and degree-2 spherical harmonic terms will be affected (Mitrovica et al., 2001, 2005). Besides, Zhou et al. (2020) found the GPS-derived low-degree spherical harmonic terms for the crustal uplift rates are quite unreliable though GPS data help to refine the terms with higher degrees. With these two reasons in mind, we decide to exclude spherical harmonic terms of degree 0, 1, and 2 in our inversion but use these terms from Zhou et al. (2020) (namely, these terms will not change). In fact, degree-0, -1, and -2 terms of GIA-induced crustal uplift rates reflect the viscosity of the deepest mantle, whereas the viscosity of the deepest mantle is better constrained by other geophysical observational data, such as the rate of degree-2 zonal term $\dot{J}_2$ or $\dot{C}_{20}$.

4.2 The Forward Problem

Here the classical VNM theory developed by Peltier and Andrews (1976) is adopted, in which the rate of radial displacement $\dot{R}(\theta, \psi, t)$ for the field point with colatitude θ and east longitude ψ at time t can be expressed as

$$\dot{R}(\theta, \psi, t) = \sum_{l=0}^{\infty} \sum_{m=-l}^{l} \dot{R}_{l,m}(t) Y_{l,m}(\theta, \psi) \tag{1}$$

where an overhead dot denotes the derivative with respect to time, $Y_{l,m}$ is the surface spherical harmonic of degree l and order m and $\dot{R}_{l,m}(t)$ is the corresponding spherical harmonic coefficients for the rate of radial displacement.

The coefficient $\dot{R}_{l,m}(t)$ is related to both the rates of the total surface mass (ice plus ocean) load $\dot{L}_{l,m}$ and the perturbing rotational potential $\dot{\Lambda}_{l,m}$, and takes the form

$$\dot{R}_{l,m}(t) = \frac{4\pi a^3}{(2l+1)M_e} \dot{L}_{l,m}(t) \otimes \Gamma_l^L(t) + \frac{\dot{\Lambda}_{l,m}(t)}{g} \otimes \Gamma_l^T(t) \tag{2}$$

where M_e, a and g are the Earth's mass, average radius and surface gravitational acceleration, respectively. The degree- and time-dependent terms $\Gamma_l^L(t)$ and $\Gamma_l^T(t)$ are coefficients in Legendre polynomial expansions for Green functions associated with radial

displacement. Mitrovica et al. (2001) showed $\Gamma_l^L(t)$ and $\Gamma_l^T(t)$ can be expressed as the sum of a series of VNMs in the form

$$\Gamma_l^L(t) = h_l^{L,E}\delta(t) + \sum_{j=1}^{J} r_j^{l,L}\exp(-s_j^l t) \tag{3a}$$

$$\Gamma_l^T(t) = h_l^{T,E}\delta(t) + \sum_{j=1}^{J} r_j^{l,T}\exp(-s_j^l t) \tag{3b}$$

where the first term on the right-hand sides of these equations denotes the instantaneous elastic response, while the second term, comprising a set of VNMs, describes the viscous response. More mathematical details for the VNM can be found in the booklet of Spada (2003a).

4.3 The Inverse Problem

In the inverse problem, we take a chi-squared analysis to quantitatively evaluate the differences between the GPS dataset and forward model predictions, and take the χ^2 value as the cost function. Our revision of viscosity profile is based on the premise that all the misfits between the GIA model predictions and GPS datasets stem from deficiencies in the radial viscosity structure, and is accomplished by editing candidate viscosity profiles to decrease the model-dataset misfits as small as possible.

The normalized χ^2 measure of misfits between N observations and predictions is computed as

$$\chi^2 = \frac{1}{N}\sum_{i=1}^{N}\frac{(O_i - C_i)^2}{\sigma_i^2} \tag{4}$$

where for the ith station, O_i and C_i are the observations (GPS-derived GIA crustal uplift rates) and computations (predictions of crustal uplift rates computed for viscosity profiles), respectively, and σ_i represents the uncertainty of the observation.

A χ^2 value of 1 indicates an appropriate trade-off between misfit and variance. A value of $\chi^2 \geq 1$ indicates that the model fits the data poorly, whereas a value of $\chi^2 \leq 1$ suggests overly conservative uncertainties or an over-parameterized model (Simon & Riva, 2020; Peltier et al., 2015).

Although a χ^2 value of 1 is usually expected in other works, we still seek the minimum of the χ^2 and corresponding viscosity profile. Here, the assigned uncertainties are just used to give different weights to different sites to constrain the mantle viscosity. The site whose quality is better plays a more important role in the revision of viscosity structure.

We have noted that GPS-derived crustal uplift rates are relatively insensitive to the variations of lithosphere related parameters, and there is a notable lateral heterogeneity in the lithosphere (e.g., Nield et al., 2018; Burov, 2011). In addition, the rheology of the lithosphere is likely to impact on the GIA-induced horizontal motions (Peltier & Drummond, 2008), which are not discussed in this study. Given these factors, we will not investigate the rheology of the lithosphere in this study. Lithosphere-related parameters (thickness of the elastic layer in the lithosphere and the viscosity with depth ranging from 60 km to 100 km) are fixed throughout the search for best-fitting models.

To overcome the trade-off among the viscosity layers in the mantle (Milne et al., 2001; Zhao et al., 2012; Argus et al., 2021), we introduced *a priori* constraints: the viscosity of lower mantle is no less than that of the upper mantle and the viscosity of lower part of lower mantle is greater than that of upper part of lower mantle (Mitrovica & Forte, 2004; Lau et al., 2016; Caron et al., 2017).

Searching for the minimum of χ^2 is accomplished by the fmincon function from the Optimization Toolbox® of MATLAB™, which can find the minimum of a constrained nonlinear multivariable function.

5 Results and Discussions

5.1 New dataset for GPS-derived GIA crustal uplift rates

Our final post-processed global GPS datasets, MIDAS-AOHS and MIDAS-AO, consisting of 2221 sites (See Figure 6 for more details), are provided in a reference frame with its origin in the CE. Sites from our datasets are mainly distributed in North America and Northwestern Eurasia, followed by Antarctica, Greenland, and South America.

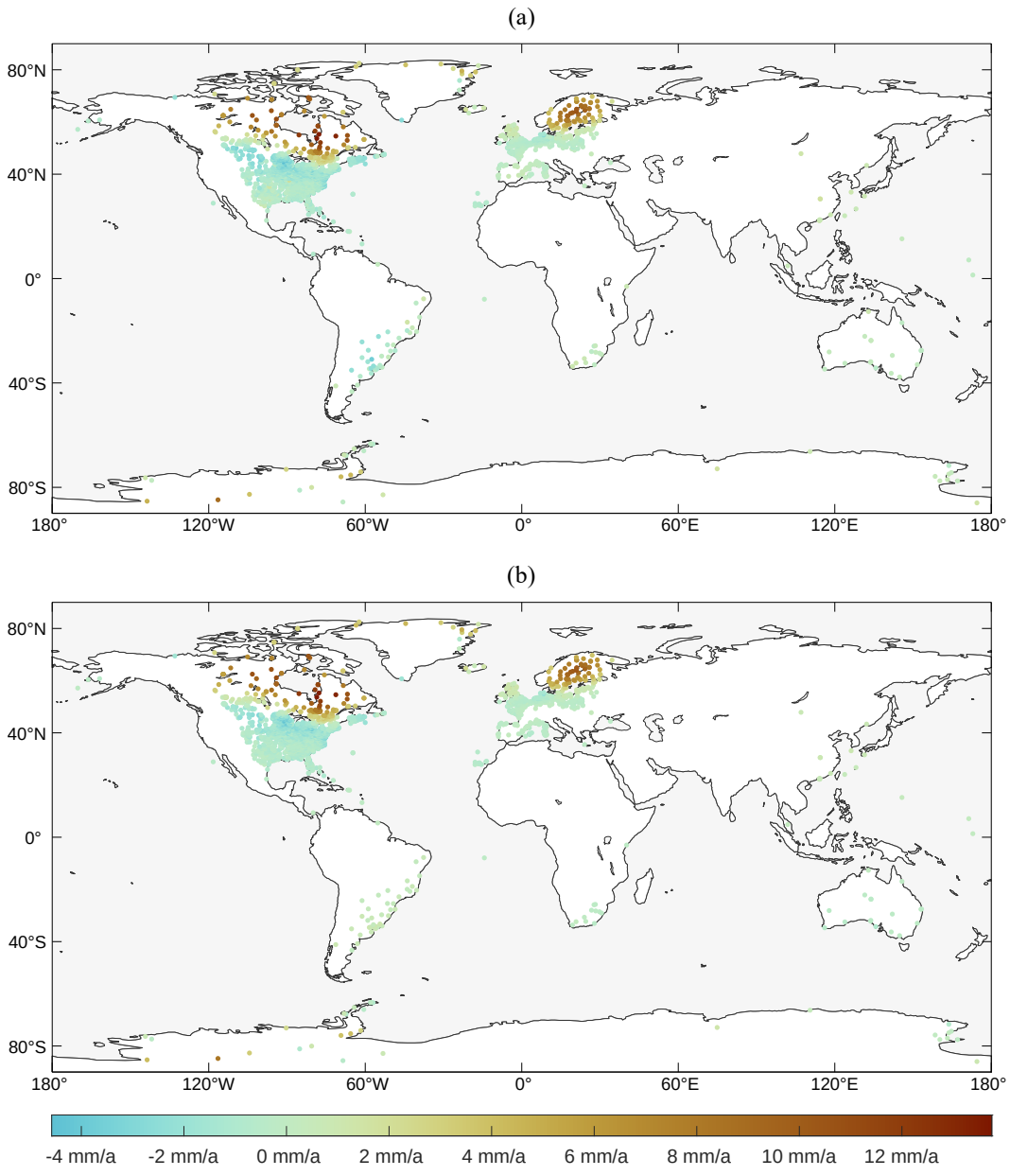

Figure 6. Distributions of the GPS sites from our GPS datasets: (a) MIDAS-AOHS; (b) MIDAS-AO. The colors of dots denote GIA crustal uplift rates.

In the following sections, we will describe and discuss our GPS datasets in the five regions of North America, Northwestern Eurasia, Antarctica, Greenland, and South America, and over the entire globe.

5.1.1 North American Continent

As illustrated in Figure 6, most sites of our GPS datasets are distributed over North America, mostly in the US with the rest scattered across Canada, especially near its southern border. The majority of places in Canada were previously covered by the Laurentide Ice Sheet and have been undergoing uplift since LGM. At the same time, most places in the US are on the periphery of the glacial bulge and thus are subsiding.

To further characterize those sites of our GPS datasets, we compute some statistical indicators (minimum, maximum, mean, and median) of our GPS datasets and GIA model predictions over the North American Continent and summarize the results in Table 2.

The minima of our GPS datasets are less than those of GIA model predictions, and the maxima of our GPS datasets are within the range of GIA model predictions. The mean and median of vertical motions for sites in North America also show that most sites in North America are still subsiding nowadays.

We can divide these sites into two groups, whether uplifting or subsiding. As for sites in the subsiding area, our GPS datasets are close to the GIA model predictions. Meanwhile, the MIDAS-AO results indicate that sites in the uplift area are generally experiencing more significant uplifting than the MIDAS-AOHS and GIA model predictions.

Figure 7 provides a clearer view of spatial differences between our GPS datasets and GIA model predictions over the North American Continent. Our GPS datasets share similar spatial differences to those of GIA model predictions, while those of GIA model predictions differ considerably. Our GPS datasets fit well with the ICE6G_D (VM5a) in the subsiding area. However, there are significant differences in the uplifting area. Compared with the ICE6G_ANU_D and the VESL 2019 models, there are pronounced differences at the forebulge of the Laurentia and within the Laurentia.

5.1.2 Northwestern Eurasia

The second most numerous concentration of sites in our datasets is in Northwest Eurasia. Most sites are located along the Atlantic coast, the Fennoscandia Peninsula, and England. In addition, a smaller number of stations fall along the Mediterranean coast.

In Northwest Eurasia, the minima of our GPS datasets are a bit less than those of GIA model predictions, and the maxima of our GPS datasets are a bit greater than those of GIA model predictions. Moreover, the mean and median values indicate that most sites in Northwest Eurasia are relatively stable.

Like North America before, we discuss the sites of our GPS sites in Northwest Eurasia separately by uplifting and subsiding areas. In the uplifting area, the results of our GPS datasets are similar to the ICE6G_D (VM5a), between the ICE6G_ANU_D and the VESL 2019. Our dataset and GIA model predictions are similar in the subsiding area (see Table 2 for more details).

As illustrated in Figure 8, in Northwestern Eurasia, our GPS datasets generally fit well with the ICE6G_D (VM5a) and the VESL 2019 models, although our GPS datasets indicate that sites in Fennoscandia Peninsula are uplifting slightly faster. Compared with the ICE6G_ANU_D, our GPS datasets indicate that sites in Fennoscandia Peninsula are uplifting about 3 mm/a faster, and sites around the Netherlands are subsiding more noticeably.

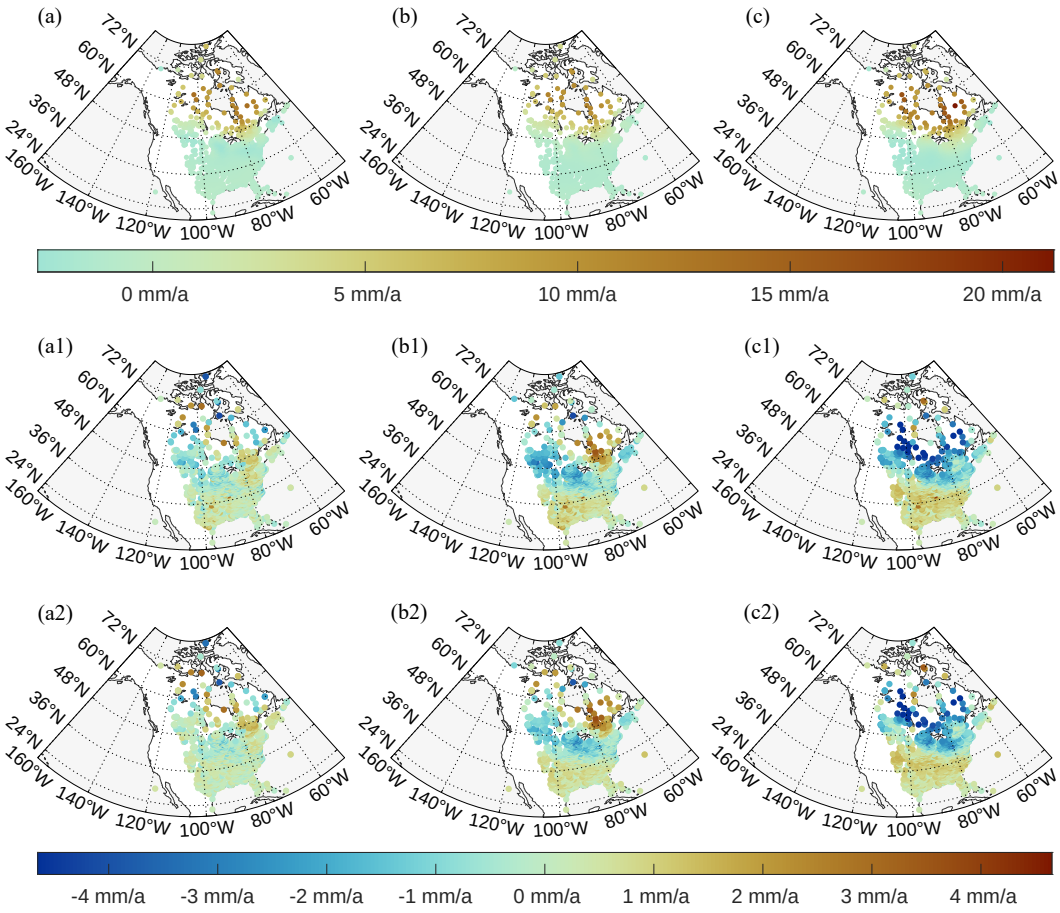

Figure 7. GIA model predictions at sites from our GPS datasets over the North American Continent and the differences of GPS rates and the GIA model rates, that is GPS minus forward model. (a) ICE6G_D (VM5a) from Peltier et al. (2018); (b) ICE6G_ANU_D from Purcell et al. (2018); (c) VESL 2019 from Caron and Ivins (2020). (a-c1) MIDAS-AOHS minus forward model predictions; (a-c2) MIDAS-AO minus forward model predictions.

Table 2. Statistics of vertical motions of sites from our GPS datasets and GIA model predictions (in mm/a) over the North American Continent and Northwestern Eurasia.

Regions	Resources	Regional Minimum	Regional Maximum	Regional Mean	Regional Median	Mean of Rising Area	Mean of Subsiding Area	Median of Rising Area	Median of Subsiding Area
North American	MIDAS-AOHS	-4.6514	13.4073	-0.6822	-1.1592	3.5917	-1.4120	2.7032	-1.3222
	MIDAS-AO	-4.5777	13.7526	-0.6487	-1.1280	4.0943	-1.3820	3.0307	-1.2662
	ICE6G_D (VM5a)	-2.7056	13.4624	-0.7131	-1.2231	3.6893	-1.3866	2.4841	-1.3119
	ICE6G_ANU_D	-1.6602	11.4045	-0.4203	-1.0449	2.9775	-1.0455	2.0310	-1.1057
	VESL 2019	-2.5484	16.4699	-0.4141	-1.4182	3.6254	-1.5021	2.5112	-1.6043
Northwestern Eurasia	MIDAS-AOHS	-2.5288	10.3087	1.0005	-0.1169	2.8569	-0.5379	1.0528	-0.4885
	MIDAS-AO	-2.4279	10.4144	1.0492	-0.1318	3.3763	-0.4378	2.1585	-0.3987
	ICE6G_D (VM5a)	-1.7191	9.6327	0.8965	-0.2052	3.1617	-0.4031	1.7997	-0.3620
	ICE6G_ANU_D	-0.5089	6.4277	0.8902	0.2667	1.4513	-0.2151	0.5790	-0.2150
	VESL 2019	-1.0567	9.1621	0.6989	-0.5451	4.0115	-0.6450	4.0361	-0.6940

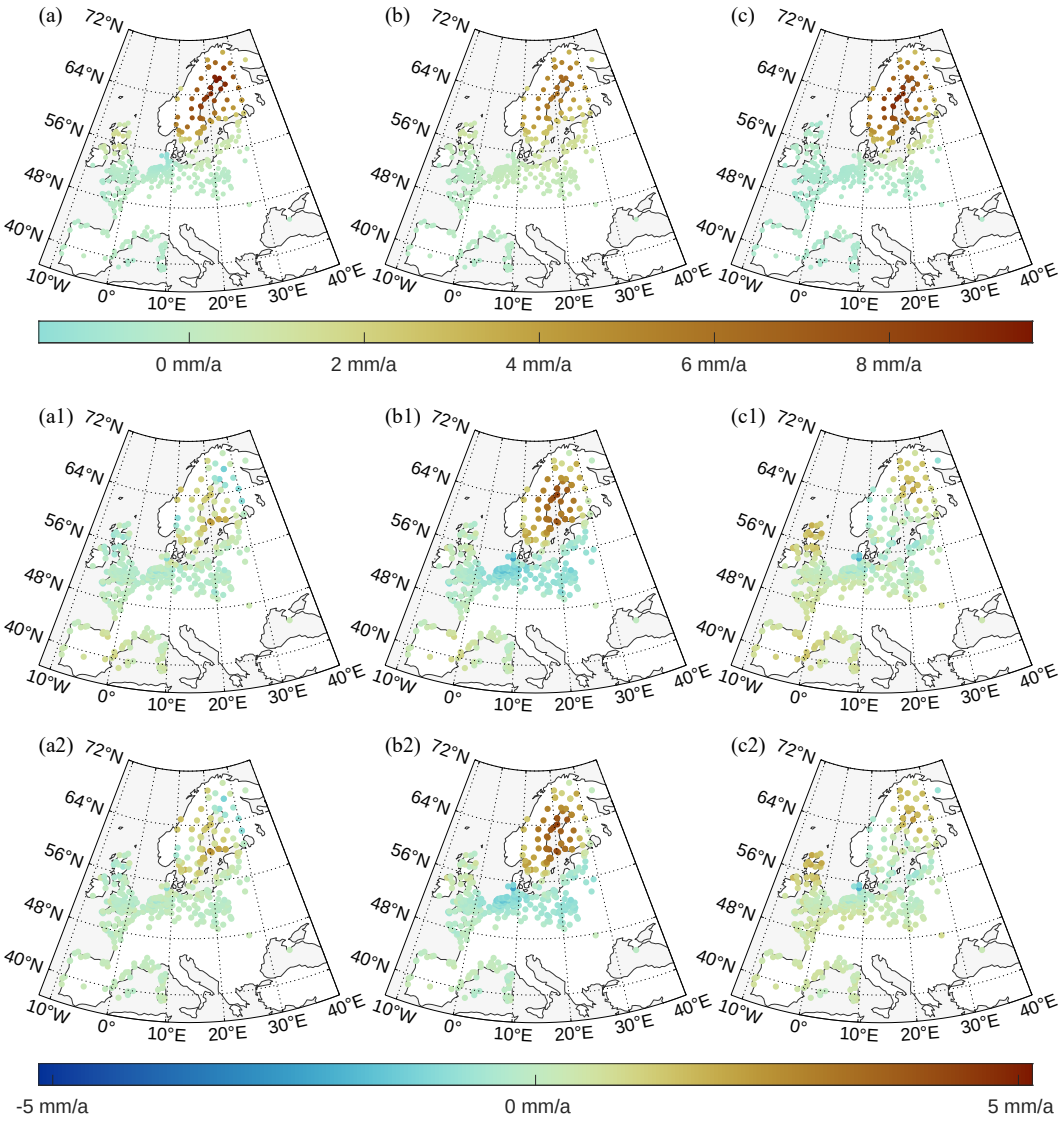

Figure 8. GIA model predictions at sites from our GPS datasets over Northwestern Eurasia and the differences of GPS rates and the GIA model rates, that is GPS minus forward model. (a) ICE6G_D (VM5a) from Peltier et al. (2018); (b) ICE6G_ANU_D from Purcell et al. (2018); (c) VESL 2019 from Caron and Ivins (2020). (a-c1) MIDAS-AOHS minus forward model predictions; (a-c2) MIDAS-AO minus forward model predictions.

5.1.3 Antarctica

As one of the three major regions of LGM ice cover, Antarctica has not been constrained as well as North America and Northwestern Eurasia. Our GPS datasets have far fewer locations in Antarctica than in North America and Northwestern Eurasia, with the majority of them concentrated in the Antarctic Peninsula and West Antarctica. At these scattered sites in Antarctica, statistical indicators show that our GPS datasets do not fit the GIA model predictions so well as those in North America and Northwestern Eurasia (see Table 3 for more details). It is notable that the ICE6G_D (VM5a) and the ICE6G_ANU_D models both indicate that all the sites in Antarctica are uplifting. In contrast, our GPS datasets and the VESL 2019 show that there are sites in Antarctica subsiding. Spatial differences are illustrated in Figure 9 show that our GPS datasets and GIA model predictions do not agree on the location of the main uplift areas in Antarctica.

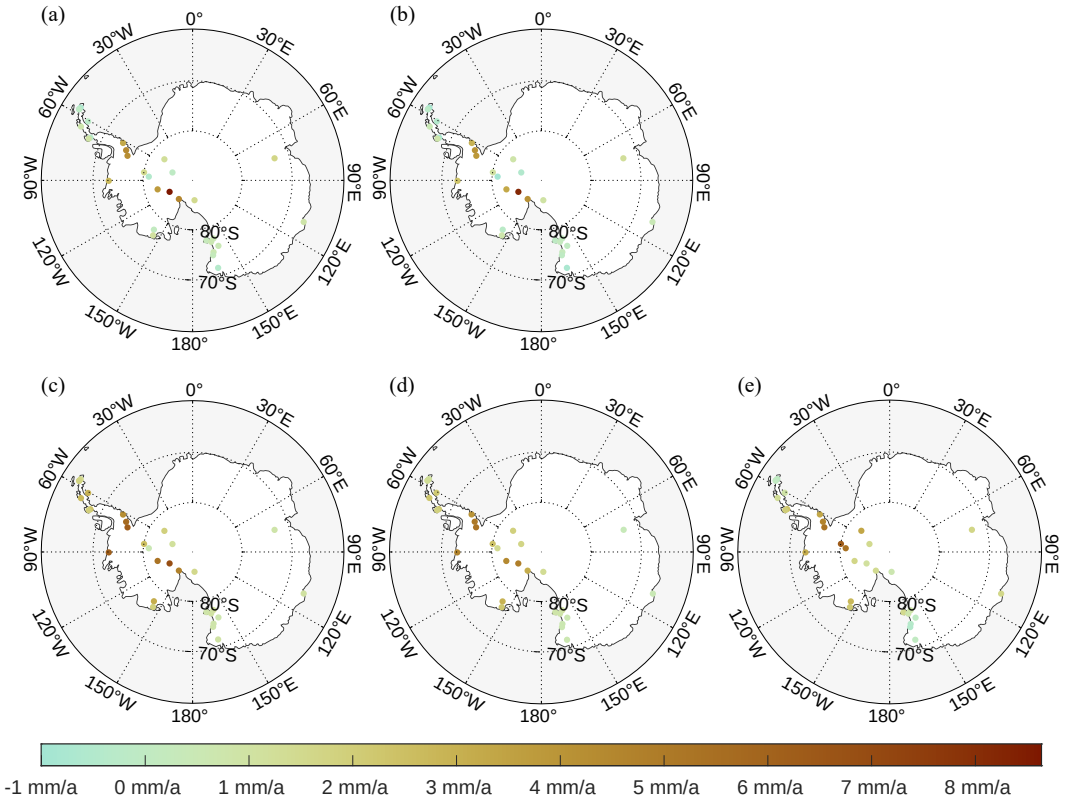

Figure 9. Comparisons between uplift rates at sites from our GPS datasets and from GIA model predictions over Antarctica. (a) MIDAS-AOHS; (b) MIDAS-AO; (c) ICE6G_D (VM5a) from Peltier et al. (2018); (d) ICE6G_ANU_D from Purcell et al. (2018); (e) VESL 2019 from Caron and Ivins (2020).

5.1.4 Greenland

In Greenland, sites are distributed on the periphery of the island, mainly at the north end. Our GPS datasets fit well with VESL 2019 and are lower overall than the ICE6G_D (VM5a) and the ICE6G_ANU_D models. Moreover, like in Antarctica before, our GPS datasets and VESL 2019 model predictions show that some sites are subsiding, while the

Table 3. Statistics of vertical motions of sites from our GPS datasets and GIA model predictions (in mm/a) over Antarctica.

Resources	Minimum	Maximum	Mean	Median
MIDAS-AOHS	-0.8754	8.6376	1.3511	0.6620
MIDAS-AO	-1.0020	8.1814	1.0044	0.3530
ICE6G_D (VM5a)	0.5335	6.8654	2.4999	1.7995
ICE6G_ANU_D	0.3243	5.3128	2.1117	1.7608
VESL 2019	-0.4653	6.3344	1.8235	1.4746

ICE6G_D (VM5a) and ICE6G_ANU_D model predictions do not. Related results are summarized in Table 4 and illustrated in Figure 10.

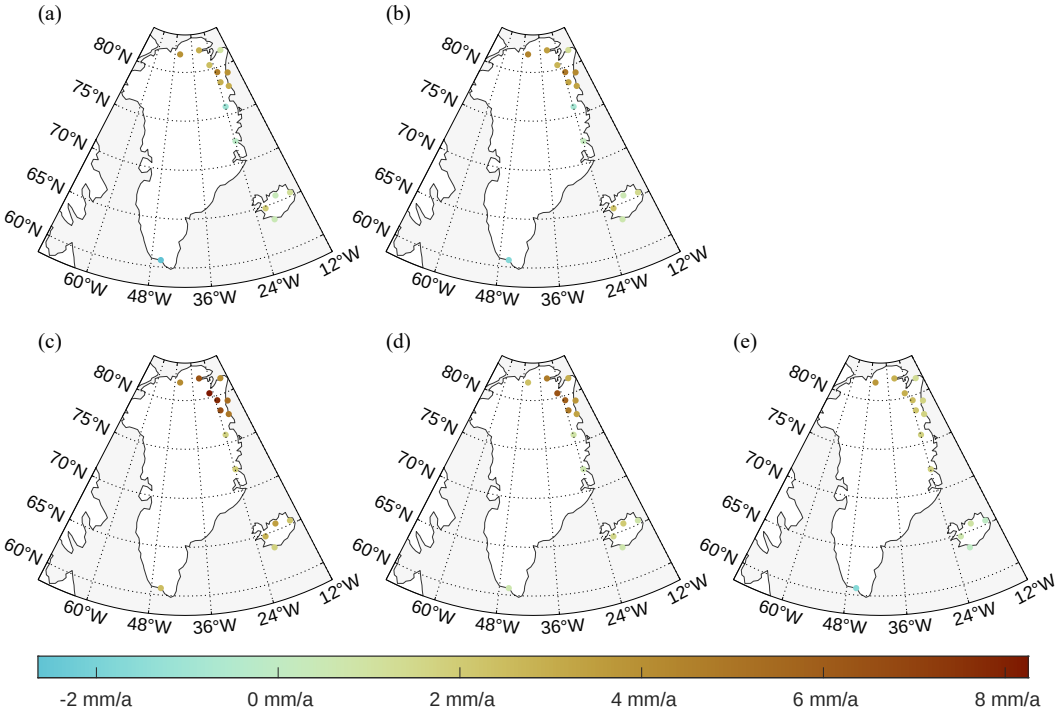

Figure 10. Comparisons between uplift rates at sites from our GPS datasets and from GIA model predictions over Greenland. (a) MIDAS-AOHS; (b) MIDAS-AO; (c) ICE6G_D (VM5a) from Peltier et al. (2018); (d) ICE6G_ANU_D from Purcell et al. (2018); (e) VESL 2019 from Caron and Ivins (2020).

5.1.5 South American Continent

Sites in South America are mainly distributed in the La Plata River Basin. Unlike sites in the glaciated regions or in the glacial forebulge regions, these sites in the far-field offer a constraint on low-degree terms of GIA fingerprints. Our GPS dataset MIDAS-AO and the three GIA model predictions are in overall good agreement. However, the GPS dataset MIDAS-AOHS differs notably from the others and is generally on the low side. Related results are summarized in Table 5 and illustrated in Figure 11. We ten-

Table 4. Statistics of vertical motions of sites from our GPS datasets and GIA model predictions (in mm/a) over Greenland.

Resources	Minimum	Maximum	Mean	Median
MIDAS-AOHS	-2.6420	4.6013	1.6391	1.9525
MIDAS-AO	-1.7452	4.9546	2.0154	2.2898
ICE6G_D (VM5a)	1.7173	8.2537	4.2461	4.0102
ICE6G_ANU_D	0.6474	6.3653	2.7540	2.3788
VESL 2019	-1.6937	3.6843	1.4734	1.6942

tatively conclude that the application of hydrological corrections may be associated with these inconsistencies. We will further discuss the causes of these inconsistencies and how they affect the inversion of the mantle's viscosities in section 5.3.

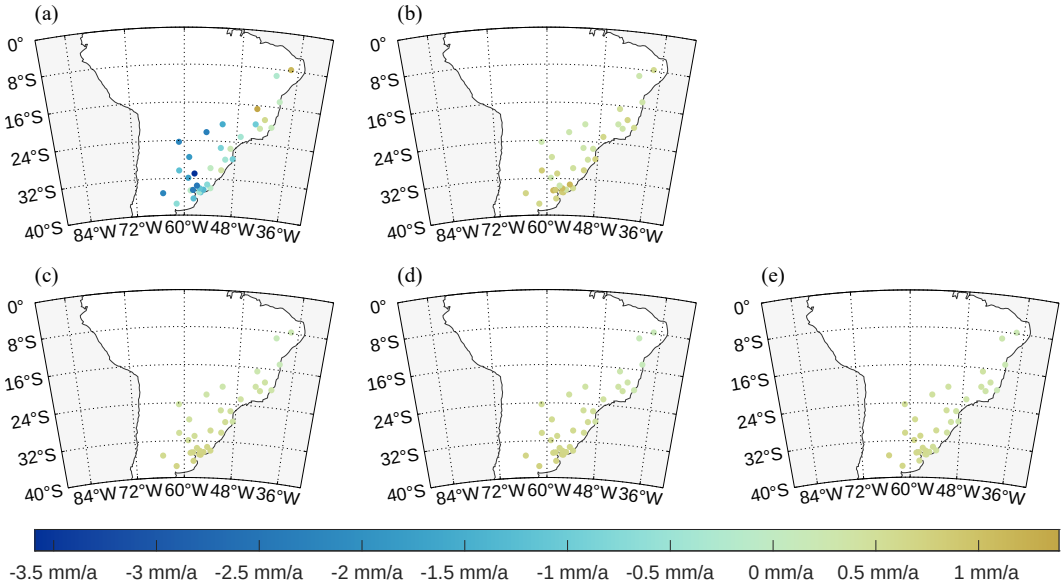

Figure 11. Comparisons between uplift rates at sites from our GPS datasets and from GIA model predictions over the South American Continent. (a) MIDAS-AOHS; (b) MIDAS-AO; (c) ICE6G_D (VM5a) from Peltier et al. (2018); (d) ICE6G_ANU_D from Purcell et al. (2018); (e) VESL 2019 from Caron and Ivins (2020).

5.1.6 Global

We further evaluated our GPS datasets with respect to the three GIA model predictions by calculating Root Mean Square (RMS) values in five regions as well as global RMS values; results are summarized in Table 6.

Adding HYDL and SLEL corrections generally brings about 0.1 mm/yr (not bigger than 0.4 mm/yr, except in South America) changes to the RMS values. In most selected regions and over the globe, MIDAS-AO fits the GIA model predictions better than MIDAS-AOHS. However, in Antarctica MIDAS-AOHS fit GIA model predictions better than MIDAS-AO. In South America, though, the HYDL and SLEL corrections increase the RMS values by about 1.7 mm/yr, which stands out compared with other re-

Table 5. Statistics of vertical motions of sites from our GPS datasets and GIA model predictions (in mm/a) over the South American Continent.

Resources	Minimum	Maximum	Mean	Median
MIDAS-AOHS	-3.5912	1.3907	-0.8225	-0.7872
MIDAS-AO	0.2427	1.1273	0.5666	0.5586
ICE6G_D (VM5a)	0.1432	0.7438	0.4893	0.4870
ICE6G_ANU_D	0.1164	0.7307	0.5073	0.5525
VESL 2019	0.2051	0.7034	0.4686	0.4936

Table 6. RMS of the vertical velocity differences (in mm/a) between our GPS datasets and GIA forward model predictions over the entire globe and five regions: North America, Northwestern Eurasia, Antarctica, Greenland, and South America.

GPS Data	GIA Model	Global	North America	Northwestern Eurasia	Antarctica	Greenland	South America
MIDAS-AOHS	ICE6G_D (VM5a)	0.7655	0.7075	0.5511	1.6331	3.0135	1.7464
	ICE6G_ANU_D	1.1300	1.0902	1.2362	1.5191	1.8103	1.7816
	VESL 2019	1.2597	1.3482	0.6452	2.3197	1.3925	1.7497
MIDAS-AO	ICE6G_D (VM5a)	0.6631	0.6182	0.5421	1.8638	2.6678	0.2272
	ICE6G_ANU_D	1.0540	1.0154	1.2448	1.6864	1.5761	0.2414
	VESL 2019	1.2187	1.3202	0.6398	2.4061	1.4660	0.2669

gions, and is thus largely likely to indicate a deficiency of HYDL (and SLEL) corrections over South America. Across near-field regions (except South America), our GPS datasets fit GIA model predictions better in North America and Northwestern Eurasia than the other regions and the globe. Improvements are needed in Antarctica and Greenland.

We next introduced the GPS dataset from Schumacher et al. (2018) into the assessment of our GPS datasets in terms of RMS and reduced χ^2 against GIA model predictions. All the results are summarized in Table 7.

Among these three GPS datasets, the MIDAS-AO always fits GIA model predictions better than the others. The vertical rates from MIDAS-AOHS and GIA model predictions agree next most closely. Across all the nine model-data pairs, the best fit is achieved by MIDAS-AO and the ICE6G_D (VM5a), whose RMS value is 0.6631 mm/yr. Against the three GIA model predictions, the RMS values of our GPS datasets are in the range of $0.6 \sim 1.3$. While the GPS dataset from Schumacher et al. (2018) shows RMS values that are greater than 1.6 with all selected GIA model predictions. In addition, concerning the results of the reduced χ^2, it is likely that the Schumacher et al. (2018) uncertainties are underestimated.

We are glad to see that the disparities of our GPS datasets against GIA model predictions are in a more acceptable range compared to the other preexisting datasets, as a result of upgrading GPS data in the IGS08 reference framework to GPS data in the IGS14 (Métivier et al., 2020), together with other processing improvements. Moreover, stricter selection of GPS sites further ensures the quality of GIA signals extracted from our GPS sites, though at the cost of coverage.

We suggest some possible explanations for the misfits enlarged due to applying the HYDL and SLEL corrections: (1) There are flaws in HYDL correction (particularly in South America); (2) GIA forward model predictions used in our studies, particularly ICE6G_D (VM5a) from Peltier et al. (2018), have already been tuned to fit GPS-derived GIA up-

Table 7. RMS and reduced χ^2 of the vertical velocity differences (in mm/a) between GPS datasets: MIDAS-AOHS, MIDAS-AO, and Schumacher et al. (2018) and GIA forward model predictions: ICE6G_D (VM5a) from Peltier et al. (2018), ICE6G_ANU_D from Purcell et al. (2018), and VESL 2019 from Caron and Ivins (2020).

GIA model prediction	GPS dataset	RMS	reduced χ^2
ICE6G_D (VM5a)	MIDAS-AOHS	0.7655	1.0757
	MIDAS-AO	0.6631	0.8483
	Schumacher et al. (2018)	1.6994	30.5026
ICE6G_ANU_D	MIDAS-AOHS	1.1300	2.4153
	MIDAS-AO	1.0540	2.1904
	Schumacher et al. (2018)	1.7968	37.2677
VESL 2019	MIDAS-AOHS	1.2597	2.6281
	MIDAS-AO	1.2187	2.6255
	Schumacher et al. (2018)	1.9385	43.4628

Table 8. Viscosity profiles of VM5aR_AO1, VM5aR_AO2, and VM5a.

Depth range km	VM5a $\times 10^{21}$ Pa s	VM5aR_AO1 $\times 10^{21}$ Pa s	VM5aR_AO2 $\times 10^{21}$ Pa s
0-60	elastic	elastic	elastic
60-100	10.0	10.0	10.0
100-420	0.50	0.62	0.51
420-670	0.50	0.62	0.71
670-1260	1.57	1.34	1.34
1260-2885.5	3.23	4.33	4.05

lift rates without hydrological corrections; and (3) SLEL is computed without considering the current-day melting of glaciers and ice sheets, so SLEL does not necessarily keep the global mass conserved after the introduction of PDMT.

Given the performance of MIDAS-AOHS in the assessments against GIA model predictions, MIDAS-AOHS will not be involved in the subsequent revision of the viscosity profiles. Only MIDAS-AO will be utilized to revise viscosity profiles.

5.2 Revised Viscosity Profiles

Combining our global GPS dataset MIDAS-AO, and nonlinear programming solver fmincon, a new radially symmetric viscosity profile VM5aR_AO1 for the Earth's mantle is presented here. Moreover, an additional viscosity structure at the transition zone (depth ranging 420 - 670 km) is tentatively introduced in our revision of the viscosity of the mantle, and another viscosity profile VM5aR_AO2 is presented. Our new viscosity profiles are illustrated in Figure 12, and their properties are listed in Table 8; more details about the modeling of these profiles including spectral responses (elastic and fluid loading Love numbers and spectra of characteristic times with a range of harmonic degrees) are illustrated in Figure S2-4. These spectral responses demonstrate that our profiles are modeled successfully (Spada et al., 2011).

Compared with the precursor model VM5a, VM5aR_AO1 indicates a stiffer upper mantle (100-670 km). As for finer structures within the upper mantle, VM5aR_AO2 shows

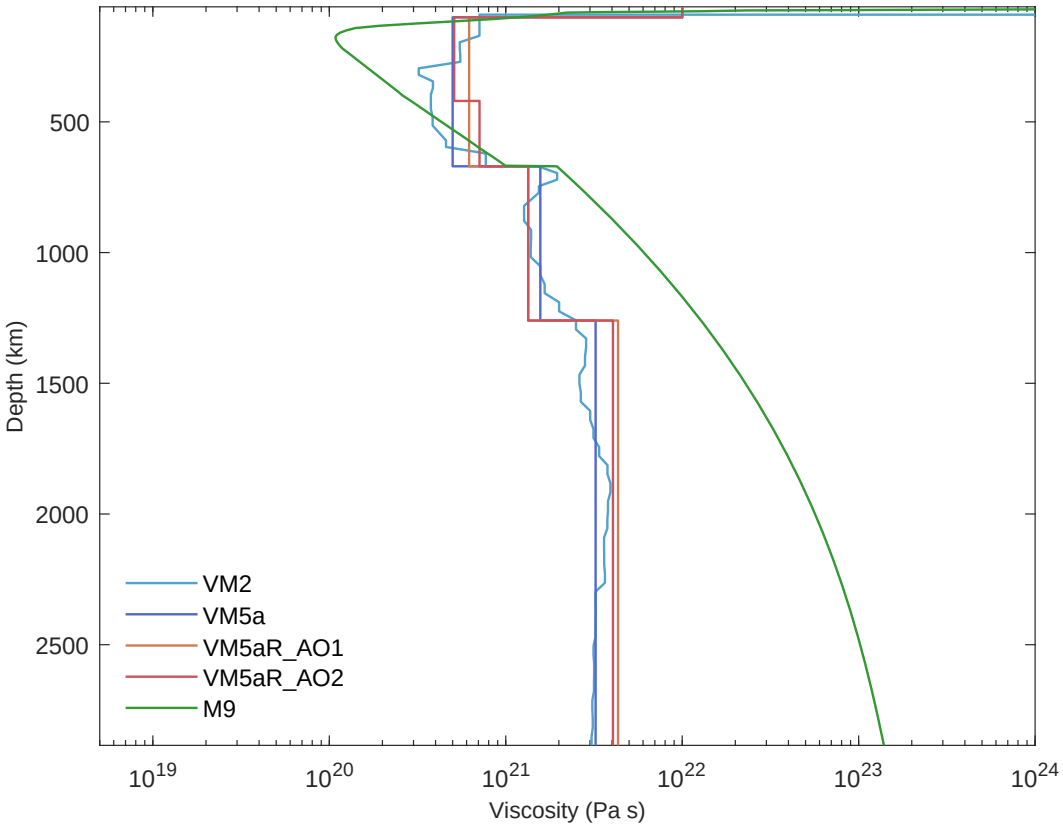

Figure 12. Comparison of the radial variations of the viscosity in depth for the VM5aR_AO1 and VM5aR_AO2 viscosity profiles with the VM5a from Argus et al. (2014), VM2 from Peltier (2004) and M9 from Nakada et al. (2018).

Table 9. Misfits of forward modeling predictions using different viscosity profiles compared to GPS datasets in terms of RMS (in mm/yr) and reduced χ^2.

GPS dataset[a]	viscosity profile[a]	RMS	reduced χ^2
MIDAS-AOHS	VM5a	0.8430	1.3503
	VM5aR_AO1	0.8349	1.3087
	VM5aR_AO2	0.8236	1.2766
MIDAS-AO	VM5a	0.7574	1.1157
	VM5aR_AO1	0.7231	1.0171
	VM5aR_AO2	0.7185	1.0069
Schumacher et al. (2018)	VM5a	1.7620	35.2840
	VM5aR_AO1	1.7859	37.0480
	VM5aR_AO2	1.7784	36.5280

[a] Spherical harmonic terms of degrees 0~2 are not included in both GPS datasets and forward modeling predictions.

a softer upper part of the upper mantle (100-420 km) and a harder transition zone (420-670 km), compared to VM5aR_AO1. This means that there is an increase of viscosity within the upper mantle, which also is supported by VM2 and M9 (Figure 12). In addition, our revised viscosity profiles indicate similarly a softer upper part of the lower mantle (670-1260 km). And a stiffer lower part of the lower mantle is preferred by our revised viscosity profiles.

Results of RMS and χ^2 of our viscosity profiles compared to the GPS uplift rates are summarized in Table 9. Not surprisingly, viscosity profile VM5aR_AO2 with an additional structure in the transition zone is found to fit the observational data better than VM5aR_AO1, as there is more room for the models with more parameters to adjust themselves to fit observational data. Additionally, our revised profiles are shown to fit the dataset MIDAS-AOHS better than the VM5a. However, when it comes to the dataset from Schumacher et al. (2018), worse results are obtained by our revised profiles.

Unfortunately, misfits maps (Figure 13) show that the model-dataset misfits of VM5a have not been eliminated decisively but rather reduced somewhat by our revised viscosity profiles. To see more clearly how our revised viscosity profiles affect the misfits, we calculated the variations of absolute model-data misfits, that is $|\dot{R}_{\mathrm{VM5aR}}-\dot{R}_{\mathrm{GPS}}|-|\dot{R}_{\mathrm{VM5a}}-\dot{R}_{\mathrm{GPS}}|$, and mapped these results in Figure 14.

Compared with the precursor VM5a, our revised viscosity profiles similarly enable better fits at sites in the Scandinavian Peninsula and between Hudson Bay and Lake Ontario. At the same time, fits to the MIDAS-AO at sites from Lake Huron to Great Slave Lake worsen in our revised profile reconstructions. The deterioration of fits at these sites in the scenario of VM5aR_AO2 is not as severe as that of VM5aR_AO1.

5.3 Sensitivity Analysis

Fréchet kernels provide a measure of the sensitivity of a datum δy to $\delta v(r)$, depth-dependent perturbations in mantle viscosity. For a given datum, we define the Fréchet kernel by the relation

$$\delta y = \int_{\mathrm{CMB}}^{\mathrm{LAB}} F(v,r)\delta v(r) r^2 dr \tag{5}$$

where CMB and LAB are the dimensionless radii of the core-mantle boundary and the lithosphere-asthenosphere boundary (or the base of the lithosphere), respectively.

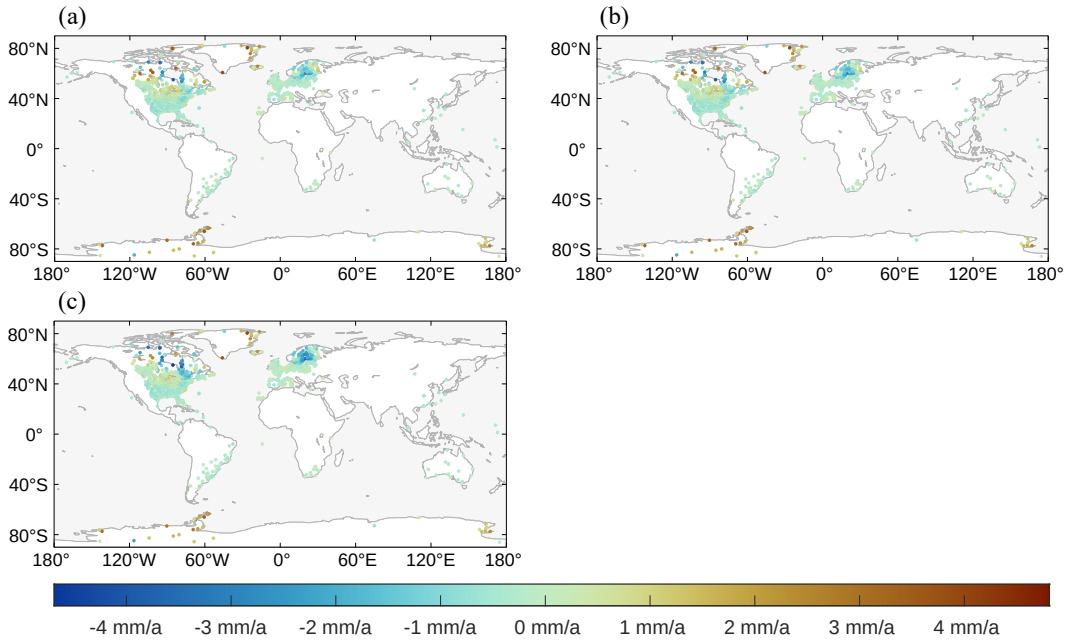

Figure 13. Misfits between forward model predictions computed by different viscosity profiles and our new GPS datasets. (a) VM5aR_AO1 - MIDAS-AO; (b) VM5aR_AO2 - MIDAS-AO; (c) VM5a - MIDAS-AO.

To be consistent with the revision of spherically symmetric models of mantle viscosity, we discretize Fréchet kernels in the same way as VM5a discretizes radial viscosity profile, and scale discrete Fréchet kernels by r^2. The discrete scaled Fréchet kernel of the ith layer $F_i r^2$ has the form

$$F_i r^2 = \frac{\delta y}{\delta v_i (r_{i+1} - r_i)} \tag{6}$$

where δv_i is the perturbation of the ith layer's viscosity, r_{i+1} and r_i are the radii of the ith layer's upper and lower boundaries, respectively.

These scaled Fréchet kernels are computed in which the viscosity of the mantle is allowed to vary, in turn, in each of the mantle subdivisions of the VM5a profile, while the rest of the profile remains identical to VM5a. Throughout the computations, the viscosity perturbation δv is set to be 0.01×10^{21} Pa s, and the ice loading history is fixed to the ICE-6G_D model.

As shown in Figure 15, scaled Fréchet kernels for crustal uplift rates (without spherical harmonic terms of degrees 0, 1, and 2) are related to the glaciation history and depths of the mantle. Stiffer mantle viscosity values tend to reproduce more pronounced uplifts in the glaciated regions and more pronounced collapses in the glacial peripheral regions, and thus more abrupt transition between the uplifting regions and the forebulge collapse regions. And we can see that the scaled Fréchet kernels for crustal uplift rates become more geographically uniform with increasing depth of the mantle.

As indicated by the magnitudes of kernels, GIA-induced crustal uplift rates are more sensitive to the viscosity variations of the upper mantle (depth ranging from 100 km to 670 km, especially the transition zone) than those of the lower mantle and lithosphere. Thus, observed uplift rates could be invoked to constrain the viscosity of the upper mantle (especially the transition zone) more reliably than those of other parts of the mantle.

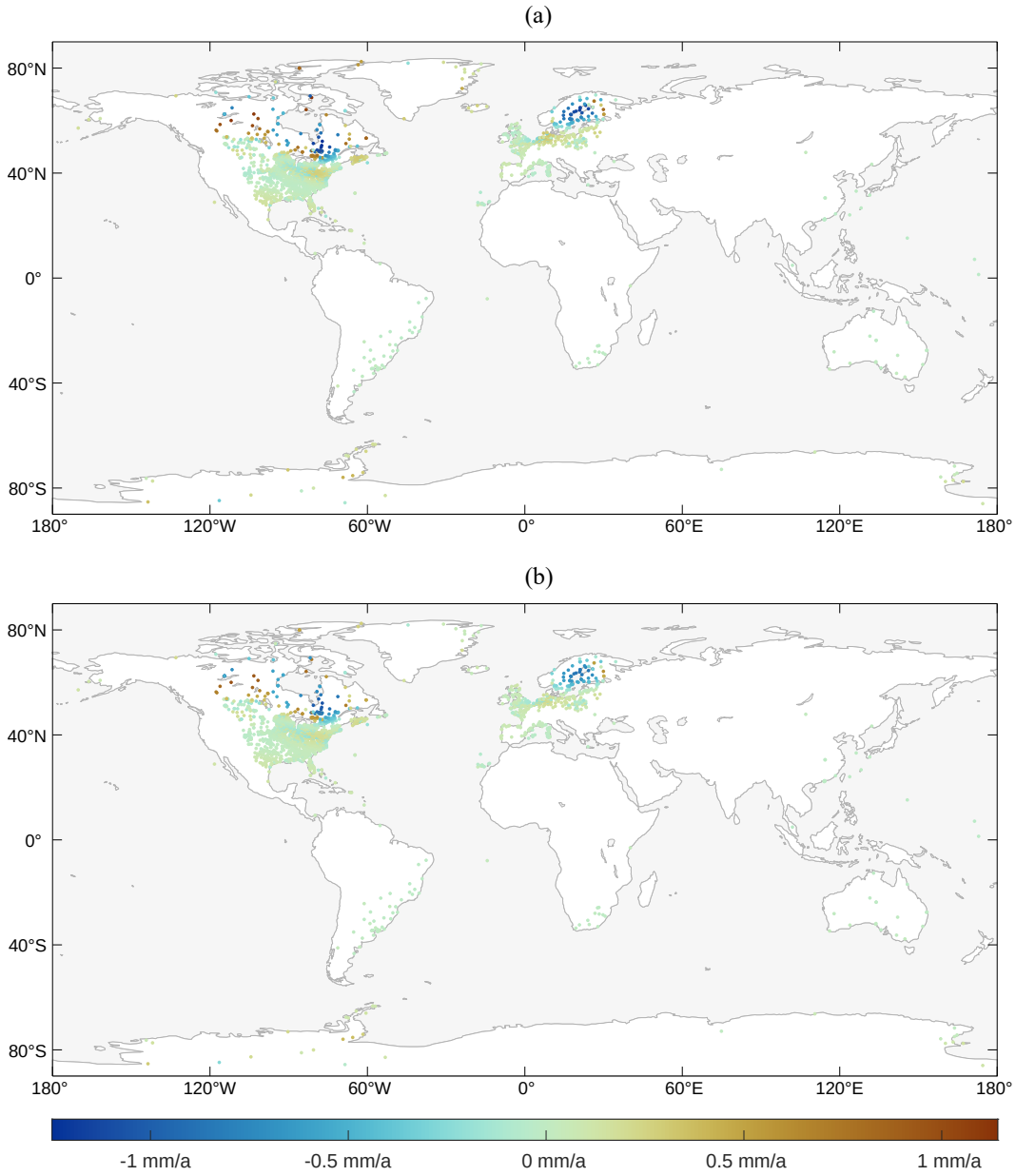

Figure 14. Changes in the absolute misfits of VM5aRx and VM5a to GPS datasets, that is $|\dot{R}_{\mathrm{VM5aR}} - \dot{R}_{\mathrm{GPS}}| - |\dot{R}_{\mathrm{VM5a}} - \dot{R}_{\mathrm{GPS}}|$.
(a) —VM5aR_AO1 - MIDAS-AO— - —VM5a - MIDAS-AO—;
(b) —VM5aR_AO2 - MIDAS-AO— - —VM5a - MIDAS-AO—.

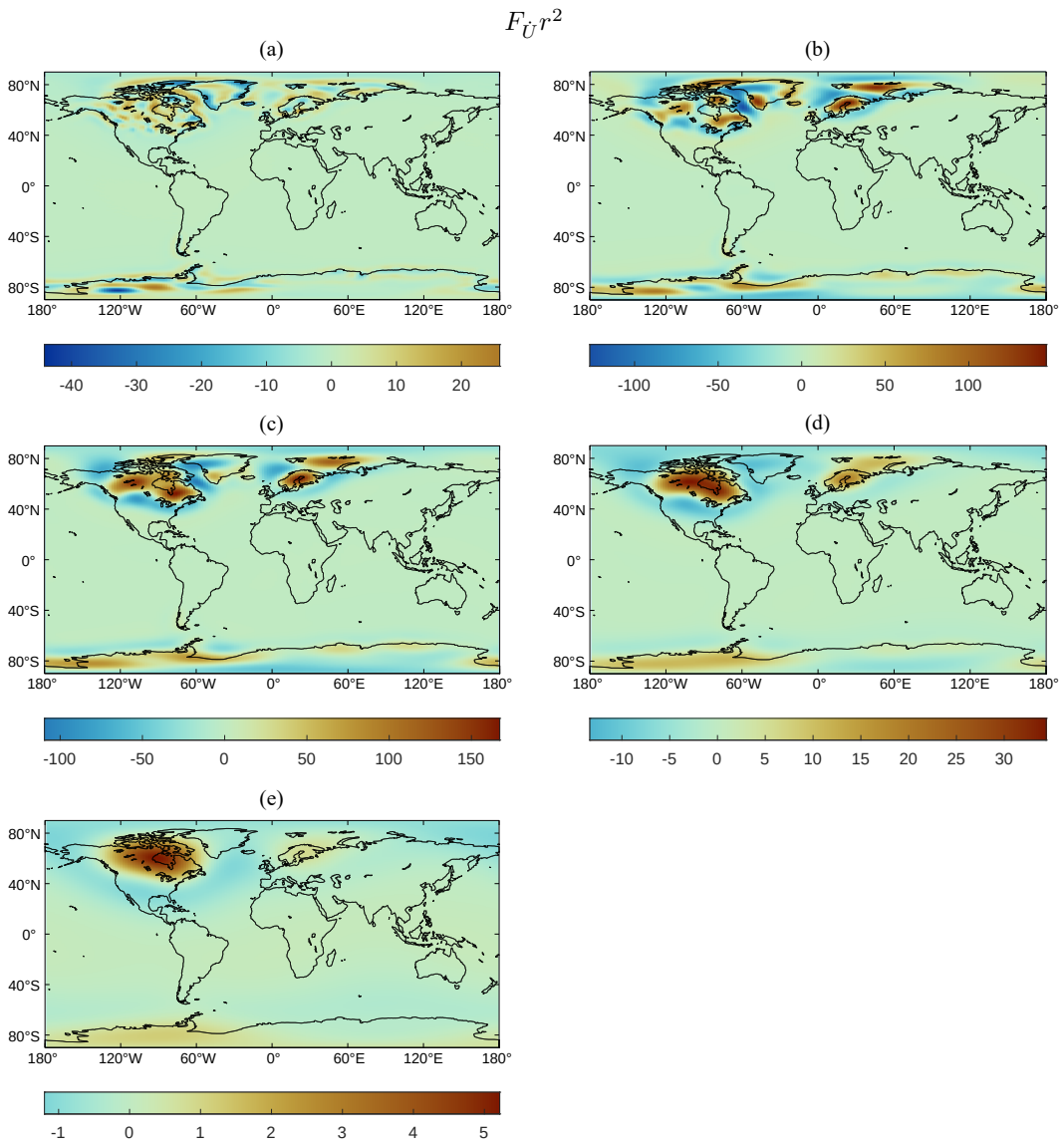

Figure 15. Dimensionless discrete Fréchet kernel (scaled by r^2) of crustal uplift rates (without spherical harmonic term of degrees 0˜2). (a) depth ranging 60-100 km; (b) depth ranging 100-420 km; (c) depth ranging 420-670 km; (d) depth ranging 670-1260 km; (e) depth ranging 1260-2885.5 km.

It should be noted that near-field uplift rates are much more sensitive to the viscosity variations of the mantle than far-field uplift rates, and within the near-field, crustal uplift rates in the glaciated region are somewhat more sensitive to the viscosity variations of the mantle than those over the forebulge. In this way, crustal uplift rates at GPS sites in the glaciated regions (and glacier forebulge regions) offer more constraints on the viscosity of the mantle via the GIA approach than those in the far-filed areas. Thus, we should be more cautious with hydrological corrections in the near-field areas (e.g., Canada, Greenland, and Antarctica) when it comes to estimating GIA signals from GPS observations.

6 Conclusions

In this study, we have presented two global GPS-derived GIA uplift rate datasets, MIDAS-AOHS (with HYDL and SLEL corrections applied) and MIDAS-AO (without HYDL and SLEL corrections applied), and subsequently utilized them to invert the mantle viscosity profile on the basis of the VM5a model, with two revised viscosity profiles, VM5aR_AO1 and VM5aR_AO2, released.

For the GPS-derived GIA uplift rates, we can conclude that our datasets (MIDAS-AOHS and MIDAS-AO) have notable improvements compared with those of Schumacher et al. (2018) (the global RMS differences between them can reach ~1 mm/yr level), since our datasets in general agree better with the GIA forward modeling results. The improvements of MIDAS-AOHS and MIDAS-AO relative to the dataset of Schumacher et al. (2018) are partly due to the adoption of MIDAS velocities in the updated global reference frame IGS14, more strict site selection criterion, and improved geophysical fluid loading products from ESMGFZ. Despite various improvements of the ESMGFZ hydrological model (together with the sea level correction model) with respect to previous ones, we found applying hydrological and sea level loading corrections can increase the RMS misfits by ~0.1 mm/yr with respect to GIA model predictions at the global scale, and ~1.5 mm/yr increase in South America. Therefore, hydrological and sea level loading corrections are still not accurate enough for GIA-related studies, and the MIDAS-AO dataset without these corrections is recommended.

The two viscosity profiles VM5aR_AO1 and VM5aR_AO2 are obtained by revising the VM5a model under the constraints of the MIDAS-AO dataset. With respect to VM5a, VM5aR_AO1 indicates a slight increase of viscosity within the upper mantle, while VM5aR_AO2 favors a softer upper part of the upper mantle and a stiffer transition zone. Maps of the variations of model-dataset misfits show that our new viscosity profiles commonly recover a better fit for sites located in the Scandinavian Peninsula and south of the Hudson Bay.

Finally, global sensitivity analyses show that GIA-induced crustal uplift rates are relatively more sensitive to the viscosity variations of the upper mantle than those of the lower mantle. Therefore, GPS-derived crustal uplift rates are more suitable for constraining the viscosity of the upper mantle, and the changes in the upper mantle indicated by our revised models VM5aR_AO1 and VM5aR_AO2 are plausible.

7 Open Research

Glaciation history ICE-6G_D is available at `https://www.atmosp.physics.utoronto.ca/~peltier/data.php`.

GIA forward model prediction ICE-6G_D (VM5a) by Peltier et al. (2018) is available at `https://www.atmosp.physics.utoronto.ca/~peltier/data.php`; ICE6G_ANU_D by Purcell et al. (2018) is available at `https://agupubs.onlinelibrary.wiley.com/action/downloadSupplement?doi=10.1002%2F2017JB014930&file=jgrb52445-sup-0003`

-supinfo.xyz; VESL 2019 by Caron and Ivins (2020) is available at https://vesl.jpl.nasa.gov/solid-earth/gia/downloads/GIA_maps_Caron_Ivins_2019.

MIDAS velocities file by NGL is available at http://geodesy.unr.edu/vlm.php. Elastic surface loading deformations by ESMGFZ are available at http://rz-vm115.gfz-potsdam.de:8080/repository. The global signature of post-1900 land ice wastage on vertical land motion by Riva et al. (2017) is available at https://doi.org/10.4121/uuid:fb667e7a-52f3-4876-8cab-ae7a2ddaf0db.

Acknowledgments

The authors declare no conflict of interest. This work was supported by the National Natural Science Foundation of China (No. 41874025 and 41474022).

References

Altamimi, Z., Rebischung, P., Métivier, L., & Collilieux, X. (2016). ITRF2014: A new release of the International Terrestrial Reference Frame modeling nonlinear station motions. *Journal of Geophysical Research: Solid Earth*, *121*(8), 6109–6131. doi: 10.1002/2016JB013098

Argus, D. F., & Peltier, W. R. (2010). Constraining models of postglacial rebound using space geodesy: A detailed assessment of model ICE-5G (VM2) and its relatives. *Geophysical Journal International*. doi: 10.1111/j.1365-246X.2010.04562.x

Argus, D. F., Peltier, W. R., Blewitt, G., & Kreemer, C. (2021). The Viscosity of the Top Third of the Lower Mantle Estimated Using GPS, GRACE, and Relative Sea Level Measurements of Glacial Isostatic Adjustment. *Journal of Geophysical Research: Solid Earth*, *126*(5). doi: 10.1029/2020JB021537

Argus, D. F., Peltier, W. R., Drummond, R., & Moore, A. W. (2014). The Antarctica component of postglacial rebound model ICE-6G_C (VM5a) based on GPS positioning, exposure age dating of ice thicknesses, and relative sea level histories. *Geophysical Journal International*, *198*(1), 537–563. doi: 10.1093/gji/ggu140

Bar-Sever, Y. E. (1996). A new model for GPS yaw attitude. *Journal of Geodesy*, *70*(11), 714–723. doi: 10.1007/BF00867149

Bassiri, S., & Hajj, G. A. (1993). Higher-order ionospheric effects on the GPS observables and means of modeling them..

Blewitt, G., Hammond, W., & Kreemer, C. (2018). Harnessing the GPS Data Explosion for Interdisciplinary Science. *Eos*, *99*. doi: 10.1029/2018EO104623

Blewitt, G., Kreemer, C., Hammond, W. C., & Gazeaux, J. (2016). MIDAS robust trend estimator for accurate GPS station velocities without step detection. *Journal of Geophysical Research: Solid Earth*, *121*(3), 2054–2068. doi: 10.1002/2015JB012552

Bock, Y., & Melgar, D. (2016). Physical applications of GPS geodesy: A review. *Reports on Progress in Physics*, *79*(10), 106801. doi: 10.1088/0034-4885/79/10/106801

Bradley, S. L., Milne, G. A., Shennan, I., & Edwards, R. (2011). An improved glacial isostatic adjustment model for the British Isles. *Journal of Quaternary Science*, *26*(5), 541–552. doi: 10.1002/jqs.1481

Burov, E. B. (2011). Rheology and strength of the lithosphere. *Marine and Petroleum Geology*, *28*(8), 1402–1443. doi: 10.1016/j.marpetgeo.2011.05.008

Caron, L., & Ivins, E. R. (2020). A baseline Antarctic GIA correction for space gravimetry. *Earth and Planetary Science Letters*, *531*, 115957. doi: 10.1016/j.epsl.2019.115957

Caron, L., Métivier, L., Greff-Lefftz, M., Fleitout, L., & Rouby, H. (2017). Inverting Glacial Isostatic Adjustment signal using Bayesian framework and two linearly

relaxing rheologies. *Geophysical Journal International*, *209*(2), 1126–1147. doi: 10.1093/gji/ggx083

Davis, J. L., Mitrovica, J. X., Scherneck, H.-G., & Fan, H. (1999). Investigations of Fennoscandian glacial isostatic adjustment using modern sea level records. *Journal of Geophysical Research: Solid Earth*, *104*(B2), 2733–2747. doi: 10.1029/1998JB900057

Dill, R. (2008). *Hydrological model LSDM for operational Earth rotation and gravity field variations* (Tech. Rep.). Deutsches GeoForschungsZentrum GFZ. doi: 10.2312/GFZ.B103-08095

Dill, R., & Dobslaw, H. (2013). Numerical simulations of global-scale high-resolution hydrological crustal deformations: HIGH-RESOLUTION HYDROLOGICAL LOADING. *Journal of Geophysical Research: Solid Earth*, *118*(9), 5008–5017. doi: 10.1002/jgrb.50353

Dill, R., & Dobslaw, H. (2019). Seasonal variations in global mean sea level and consequences on the excitation of length-of-day changes. *Geophysical Journal International*, *218*(2), 801–816. doi: 10.1093/gji/ggz201

Dill, R., Klemann, V., & Dobslaw, H. (2018). Relocation of River Storage From Global Hydrological Models to Georeferenced River Channels for Improved Load-Induced Surface Displacements. *Journal of Geophysical Research: Solid Earth*, *123*(8), 7151–7164. doi: 10.1029/2018JB016141

Dobslaw, H., Bergmann-Wolf, I., Dill, R., Poropat, L., Thomas, M., Dahle, C., ... Flechtner, F. (2017). A new high-resolution model of non-tidal atmosphere and ocean mass variability for de-aliasing of satellite gravity observations: AOD1B RL06. *Geophysical Journal International*, *211*(1), 263–269. doi: 10.1093/gji/ggx302

Döll, P., Müller Schmied, H., Schuh, C., Portmann, F. T., & Eicker, A. (2014). Global-scale assessment of groundwater depletion and related groundwater abstractions: Combining hydrological modeling with information from well observations and GRACE satellites. *Water Resources Research*, *50*(7), 5698–5720. doi: 10.1002/2014WR015595

Dziewonski, A. M., & Anderson, D. L. (1981). Preliminary reference Earth model. *Physics of the Earth and Planetary Interiors*, *25*(4), 297–356. doi: 10.1016/0031-9201(81)90046-7

Jungclaus, J. H., Fischer, N., Haak, H., Lohmann, K., Marotzke, J., Matei, D., ... von Storch, J. S. (2013). Characteristics of the ocean simulations in the Max Planck Institute Ocean Model (MPIOM) the ocean component of the MPI-Earth system model. *Journal of Advances in Modeling Earth Systems*, *5*(2), 422–446. doi: 10.1002/jame.20023

Karato, S.-i. (2010). Rheology of the Earth's mantle: A historical review. *Gondwana Research*, *18*(1), 17–45. doi: 10.1016/j.gr.2010.03.004

Kedar, S., Hajj, G. A., Wilson, B. D., & Heflin, M. B. (2003). The effect of the second order GPS ionospheric correction on receiver positions. *Geophysical Research Letters*, *30*(16). doi: 10.1029/2003GL017639

Kennett, B. L. N., Engdahl, E. R., & Buland, R. (1995). Constraints on seismic velocities in the Earth from traveltimes. *Geophysical Journal International*, *122*(1), 108–124. doi: 10.1111/j.1365-246X.1995.tb03540.x

King, M. A., Altamimi, Z., Boehm, J., Bos, M., Dach, R., Elosegui, P., ... Willis, P. (2010). Improved Constraints on Models of Glacial Isostatic Adjustment: A Review of the Contribution of Ground-Based Geodetic Observations. *Surveys in Geophysics*, *31*(5), 465–507. doi: 10.1007/s10712-010-9100-4

King, M. A., Keshin, M., Whitehouse, P. L., Thomas, I. D., Milne, G., & Riva, R. E. M. (2012). Regional biases in absolute sea-level estimates from tide gauge data due to residual unmodeled vertical land movement: REGIONAL BIASES IN ABSOLUTE SEA-LEVEL. *Geophysical Research Letters*, *39*(14). doi: 10.1029/2012GL052348

King, S. D. (1995). The viscosity structure of the mantle. *Reviews of Geophysics*, *33*(S1), 11–17. doi: 10.1029/95RG00279

Klos, A., Dobslaw, H., Dill, R., & Bogusz, J. (2021). Identifying the sensitivity of GPS to non-tidal loadings at various time resolutions: Examining vertical displacements from continental Eurasia. *GPS Solutions*, *25*(3), 89. doi: 10.1007/s10291-021-01135-w

Kreemer, C., Blewitt, G., & Klein, E. C. (2014). A geodetic plate motion and Global Strain Rate Model. *Geochemistry, Geophysics, Geosystems*, *15*(10), 3849–3889. doi: 10.1002/2014GC005407

Lambeck, K., Purcell, A., & Zhao, S. (2017). The North American Late Wisconsin ice sheet and mantle viscosity from glacial rebound analyses. *Quaternary Science Reviews*, *158*, 172–210. doi: 10.1016/j.quascirev.2016.11.033

Lau, H. C. P., Mitrovica, J. X., Austermann, J., Crawford, O., Al-Attar, D., & Latychev, K. (2016). Inferences of mantle viscosity based on ice age data sets: Radial structure: RADIAL VISCOSITY PROFILES. *Journal of Geophysical Research: Solid Earth*, *121*(10), 6991–7012. doi: 10.1002/2016JB013043

Martens, H. R., Argus, D. F., Norberg, C., Blewitt, G., Herring, T. A., Moore, A. W., ... Kreemer, C. (2020). Atmospheric pressure loading in GPS positions: Dependency on GPS processing methods and effect on assessment of seasonal deformation in the contiguous USA and Alaska. *Journal of Geodesy*, *94*(12), 115. doi: 10.1007/s00190-020-01445-w

Melini, D., & Spada, G. (2019). Some remarks on Glacial Isostatic Adjustment modelling uncertainties. *Geophysical Journal International*, *218*(1), 401–413. doi: 10.1093/gji/ggz158

Métivier, L., Altamimi, Z., & Rouby, H. (2020). Past and present ITRF solutions from geophysical perspectives. *Advances in Space Research*, *65*(12), 2711–2722. doi: 10.1016/j.asr.2020.03.031

Milne, G. A., Davis, J. L., Mitrovica, J. X., Scherneck, H.-G., Johansson, J. M., Vermeer, M., & Koivula, H. (2001). Space-Geodetic Constraints on Glacial Isostatic Adjustment in Fennoscandia. *Science*, *291*(5512), 2381–2385. doi: 10.1126/science.1057022

Mitrovica, J. X., & Forte, A. M. (2004). A new inference of mantle viscosity based upon joint inversion of convection and glacial isostatic adjustment data. *Earth and Planetary Science Letters*, *225*(1), 177–189. doi: 10.1016/j.epsl.2004.06.005

Mitrovica, J. X., Milne, G. A., & Davis, J. L. (2001). Glacial isostatic adjustment on a rotating earth. *Geophysical Journal International*, *147*(3), 562–578. doi: 10.1046/j.1365-246x.2001.01550.x

Mitrovica, J. X., Wahr, J., Matsuyama, I., & Paulson, A. (2005). The rotational stability of an ice-age earth. *Geophysical Journal International*, *161*(2), 491–506. doi: 10.1111/j.1365-246X.2005.02609.x

Moyer, T. D. (2003). *Formulation for Observed and Computed Values of Deep Space Network Data Types for Navigation: Moyer/Deep Space Network Data Types.* Hoboken, NJ, USA: John Wiley & Sons, Inc. doi: 10.1002/0471728470

Nakada, M., Okuno, J., & Irie, Y. (2018). Inference of viscosity jump at 670 km depth and lower mantle viscosity structure from GIA observations. *Geophysical Journal International*, *212*(3), 2206–2225. doi: 10.1093/gji/ggx519

Nield, G. A., Whitehouse, P. L., van der Wal, W., Blank, B., O'Donnell, J. P., & Stuart, G. W. (2018). The impact of lateral variations in lithospheric thickness on glacial isostatic adjustment in West Antarctica. *Geophysical Journal International*, *214*(2), 811–824. doi: 10.1093/gji/ggy158

Peltier, W. R. (2004). Global glacial isostasy and the surface of the ice-age earth: The ice-5g (vm2) model and grace. *Annual Review of Earth and Planetary Sciences*, *32*(1), 111–149. doi: 10.1146/annurev.earth.32.082503.144359

Peltier, W. R., & Andrews, J. T. (1976). Glacial-Isostatic Adjustment-I. The for-

ward problem. *Geophysical Journal of the Royal Astronomical Society*, *46*(3), 605–646. doi: 10.1111/j.1365-246X.1976.tb01251.x

Peltier, W. R., Argus, D. F., & Drummond, R. (2015). Space geodesy constrains ice age terminal deglaciation: The global ICE-6G_C (VM5a) model: Global Glacial Isostatic Adjustment. *Journal of Geophysical Research: Solid Earth*, *120*(1), 450–487. doi: 10.1002/2014JB011176

Peltier, W. R., Argus, D. F., & Drummond, R. (2018). Comment on "An Assessment of the ICE-6G_C (VM5a) Glacial Isostatic Adjustment Model" by Purcell et al.: The ICE-6G_C (VM5a) GIA model. *Journal of Geophysical Research: Solid Earth*, *123*(2), 2019–2028. doi: 10.1002/2016JB013844

Peltier, W. R., & Drummond, R. (2008). Rheological stratification of the lithosphere: A direct inference based upon the geodetically observed pattern of the glacial isostatic adjustment of the North American continent. *Geophysical Research Letters*, *35*(16), L16314. doi: 10.1029/2008GL034586

Purcell, A., Tregoning, P., & Dehecq, A. (2016). An assessment of the ICE6G_C(VM5a) glacial isostatic adjustment model. *Journal of Geophysical Research: Solid Earth*, *121*(5), 3939–3950. doi: 10.1002/2015JB012742

Purcell, A., Tregoning, P., & Dehecq, A. (2018). Reply to Comment by W. R. Peltier, D. F. Argus, and R. Drummond on "An Assessment of the ICE6G_C (VM5a) Glacial Isostatic Adjustment Model": REPLY TO COMMENT BY PELTIER ET AL. *Journal of Geophysical Research: Solid Earth*, *123*(2), 2029–2032. doi: 10.1002/2017JB014930

Riva, R. E. M., Frederikse, T., King, M. A., Marzeion, B., & van den Broeke, M. R. (2017). Brief communication: The global signature of post-1900 land ice wastage on vertical land motion. *The Cryosphere*, *11*(3), 1327–1332. doi: 10.5194/tc-11-1327-2017

Roy, K., & Peltier, W. (2015). Glacial isostatic adjustment, relative sea level history and mantle viscosity: Reconciling relative sea level model predictions for the U.S. East coast with geological constraints. *Geophysical Journal International*, *201*(2), 1156–1181. doi: 10.1093/gji/ggv066

Roy, K., & Peltier, W. (2018). Relative sea level in the Western Mediterranean basin: A regional test of the ICE-7G_NA (VM7) model and a constraint on late Holocene Antarctic deglaciation. *Quaternary Science Reviews*, *183*, 76–87. doi: 10.1016/j.quascirev.2017.12.021

Santamaría-Gómez, A., & Mémin, A. (2015). Geodetic secular velocity errors due to interannual surface loading deformation. *Geophysical Journal International*, *202*(2), 763–767. doi: 10.1093/gji/ggv190

Schumacher, M., King, M. A., Rougier, J., Sha, Z., Khan, S. A., & Bamber, J. L. (2018). A new global GPS data set for testing and improving modelled GIA uplift rates. *Geophysical Journal International*, *214*(3), 2164–2176. doi: 10.1093/gji/ggy235

Sibois, A., Selle, C., Desai, S., Sibthorpe, A., & Weiss, J. (2014). GSPM13: An updated empirical model for solar radiation pressure forces acting on GPS satellites. In *IGS workshop*.

Simon, K. M., & Riva, R. E. M. (2020). Uncertainty Estimation in Regional Models of Long-Term GIA Uplift and Sea Level Change: An Overview. *Journal of Geophysical Research: Solid Earth*, *125*(8). doi: 10.1029/2019JB018983

Simon, K. M., Riva, R. E. M., & Vermeersen, L. L. A. (2021). Constraint of glacial isostatic adjustment in the North Sea with geological relative sea level and GNSS vertical land motion data. *Geophysical Journal International*, *227*(2), 1168–1180. doi: 10.1093/gji/ggab261

Spada, G. (2003a). *TABOO - User guide*. USA and Samizdat Press.

Spada, G. (2003b). *The theory behind TABOO - a posT glAcial reBOund calculatOr*. USA and Samizdat Press.

Spada, G. (2017). Glacial Isostatic Adjustment and Contemporary Sea Level Rise:

An Overview. *Surveys in Geophysics*, *38*(1), 153–185. doi: 10.1007/s10712-016-9379-x

Spada, G., Barletta, V. R., Klemann, V., Riva, R. E. M., Martinec, Z., Gasperini, P., ... King, M. A. (2011). A benchmark study for glacial isostatic adjustment codes: A GIA benchmark study. *Geophysical Journal International*, *185*(1), 106–132. doi: 10.1111/j.1365-246X.2011.04952.x

Spada, G., & Melini, D. (2019). On Some Properties of the Glacial Isostatic Adjustment Fingerprints. *Water*, *11*(9), 1844. doi: 10.3390/w11091844

Steffen, H., & Wu, P. (2011). Glacial isostatic adjustment in Fennoscandia—A review of data and modeling. *Journal of Geodynamics*, *52*(3), 169–204. doi: 10.1016/j.jog.2011.03.002

Steffen, H., Wu, P., & Wang, H. (2010). Determination of the Earth's structure in Fennoscandia from GRACE and implications for the optimal post-processing of GRACE data. *Geophysical Journal International*, *182*(3), 1295–1310. doi: 10.1111/j.1365-246X.2010.04718.x

Whitehouse, P. L. (2018). Glacial isostatic adjustment modelling: Historical perspectives, recent advances, and future directions. *Earth Surface Dynamics*, *6*(2), 401–429. doi: 10.5194/esurf-6-401-2018

Whitehouse, P. L., Bentley, M. J., Milne, G. A., King, M. A., & Thomas, I. D. (2012). A new glacial isostatic adjustment model for Antarctica: Calibrated and tested using observations of relative sea-level change and present-day uplift rates. *Geophysical Journal International*, *190*(3), 1464–1482. doi: 10.1111/j.1365-246X.2012.05557.x

Zhao, S., Lambeck, K., & Lidberg, M. (2012). Lithosphere thickness and mantle viscosity inverted from GPS-derived deformation rates in Fennoscandia: Lithosphere thickness and mantle viscosity. *Geophysical Journal International*, *190*(1), 278–292. doi: 10.1111/j.1365-246X.2012.05454.x

Zhou, Y., Yang, S., Luo, J., Ray, J., Huang, Y., & Li, J. (2020). Global Glacial Isostatic Adjustment Constrained by GPS Measurements: Spherical Harmonic Analyses of Uplifts and Geopotential Variations. *Remote Sensing*, *12*(7), 1209. doi: 10.3390/rs12071209

Figure 1.

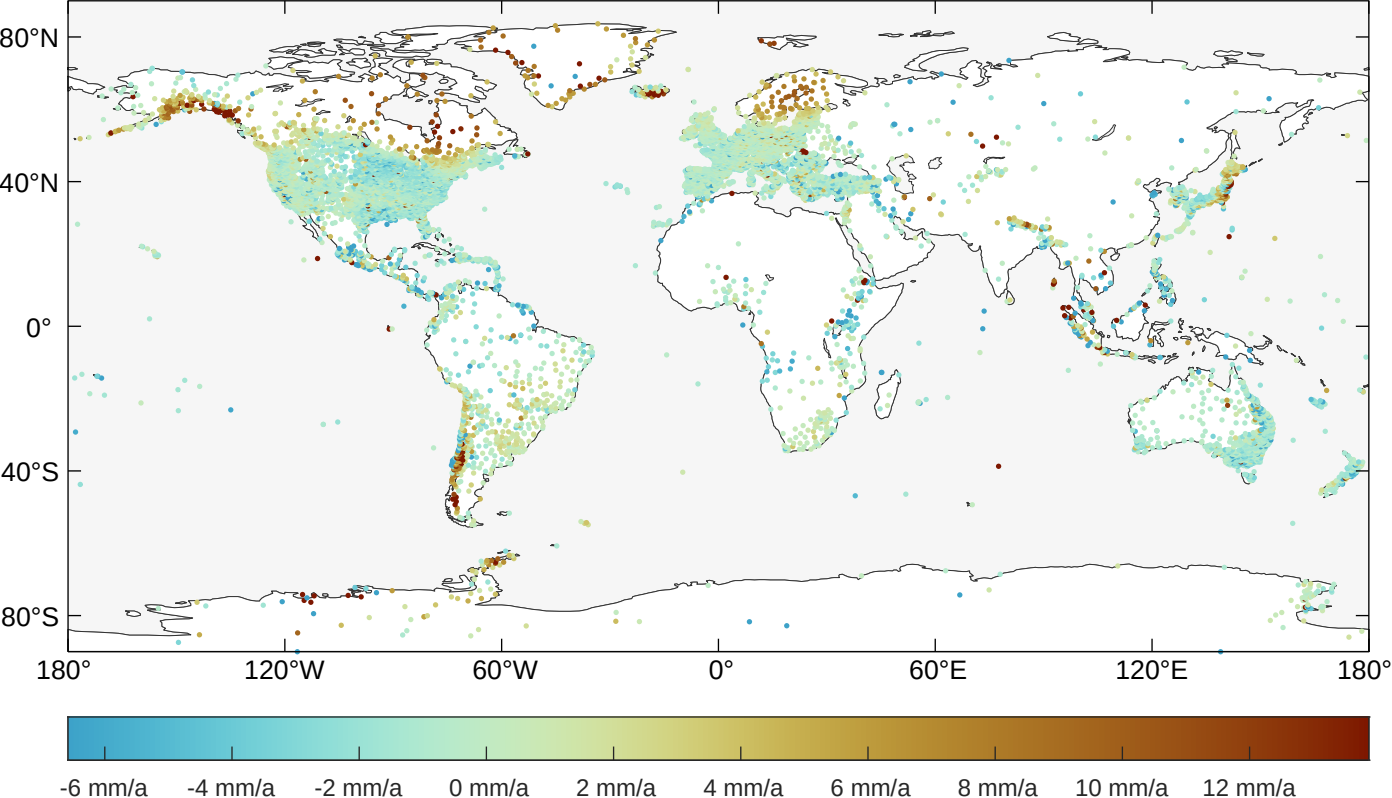
80°N
40°N
0°
40°S
80°S
180°
120°W
60°W
0°
60°E
120°E
180°
-6 mm/a
-4 mm/a
-2 mm/a
0 mm/a
2 mm/a
4 mm/a
6 mm/a
8 mm/a
10 mm/a
12 mm/a

Figure 2.

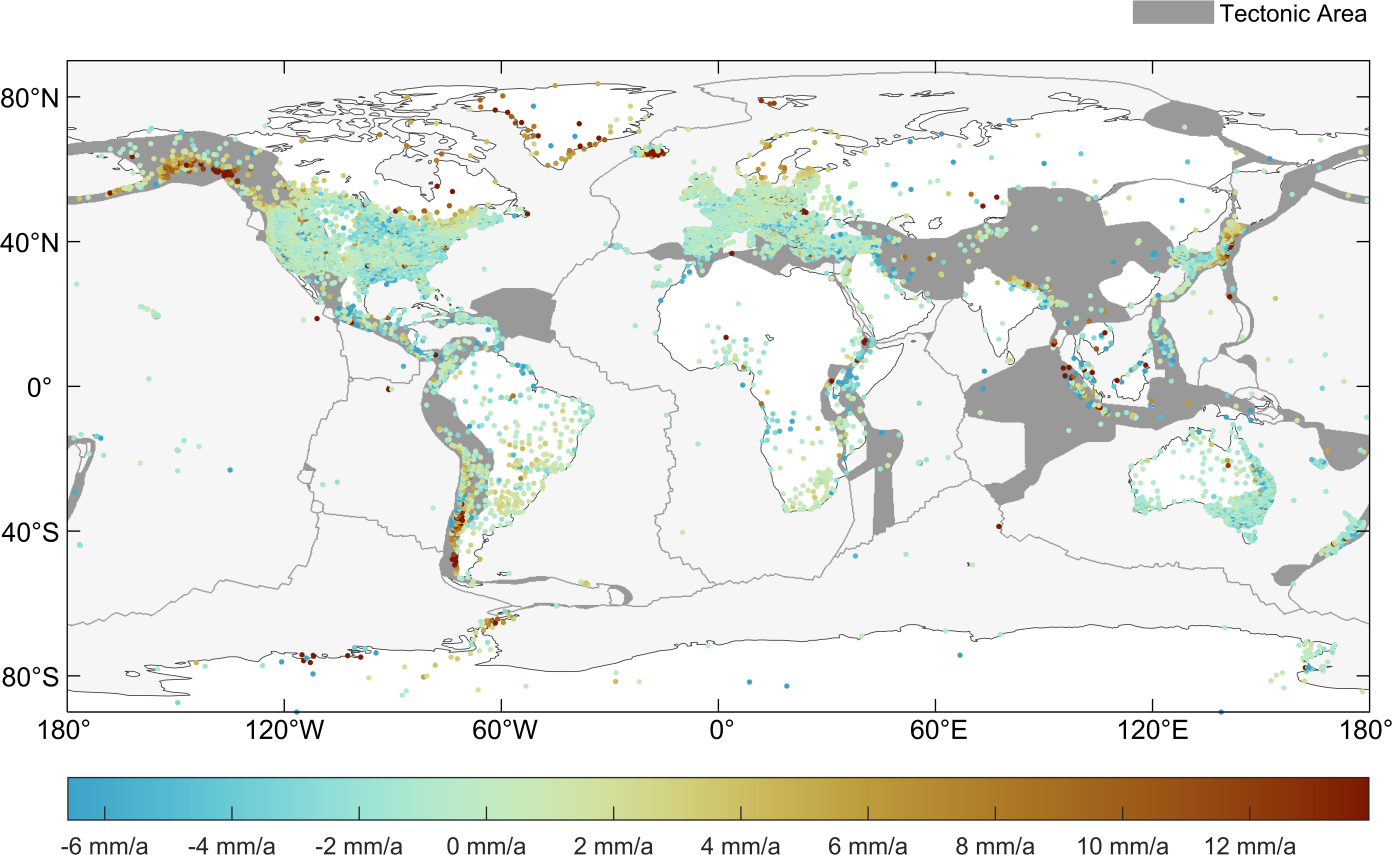
Tectonic Area
80°N
40°N
0°
40°S
80°S
180°
120°W
60°W
0°
60°E
120°E
180°
-6 mm/a
-4 mm/a
-2 mm/a
0 mm/a
2 mm/a
4 mm/a
6 mm/a
8 mm/a
10 mm/a
12 mm/a

Figure 3.

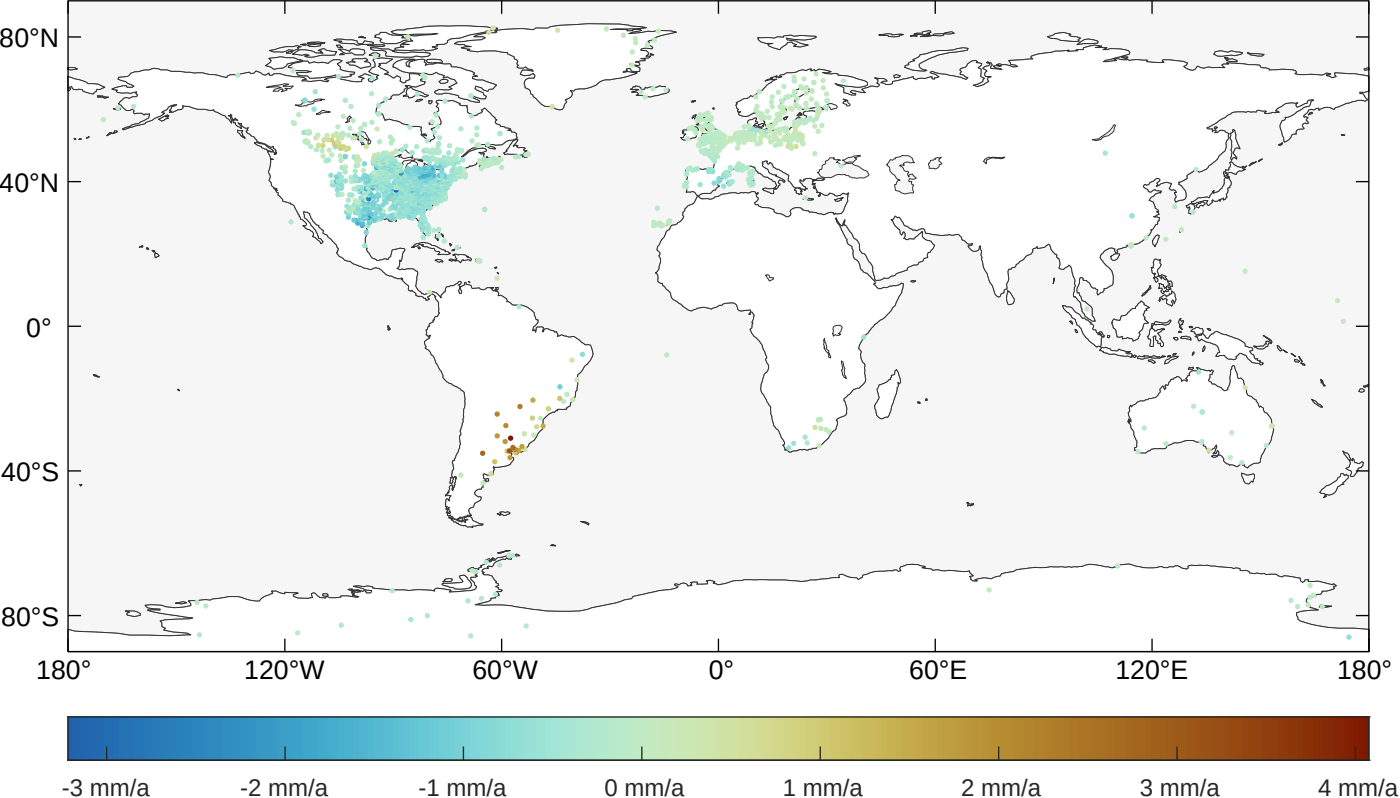
80°N
40°N
0°
40°S
80°S
180°
120°W
60°W
0°
60°E
120°E
180°
-3 mm/a
-2 mm/a
-1 mm/a
0 mm/a
1 mm/a
2 mm/a
3 mm/a
4 mm/a

Figure 4.

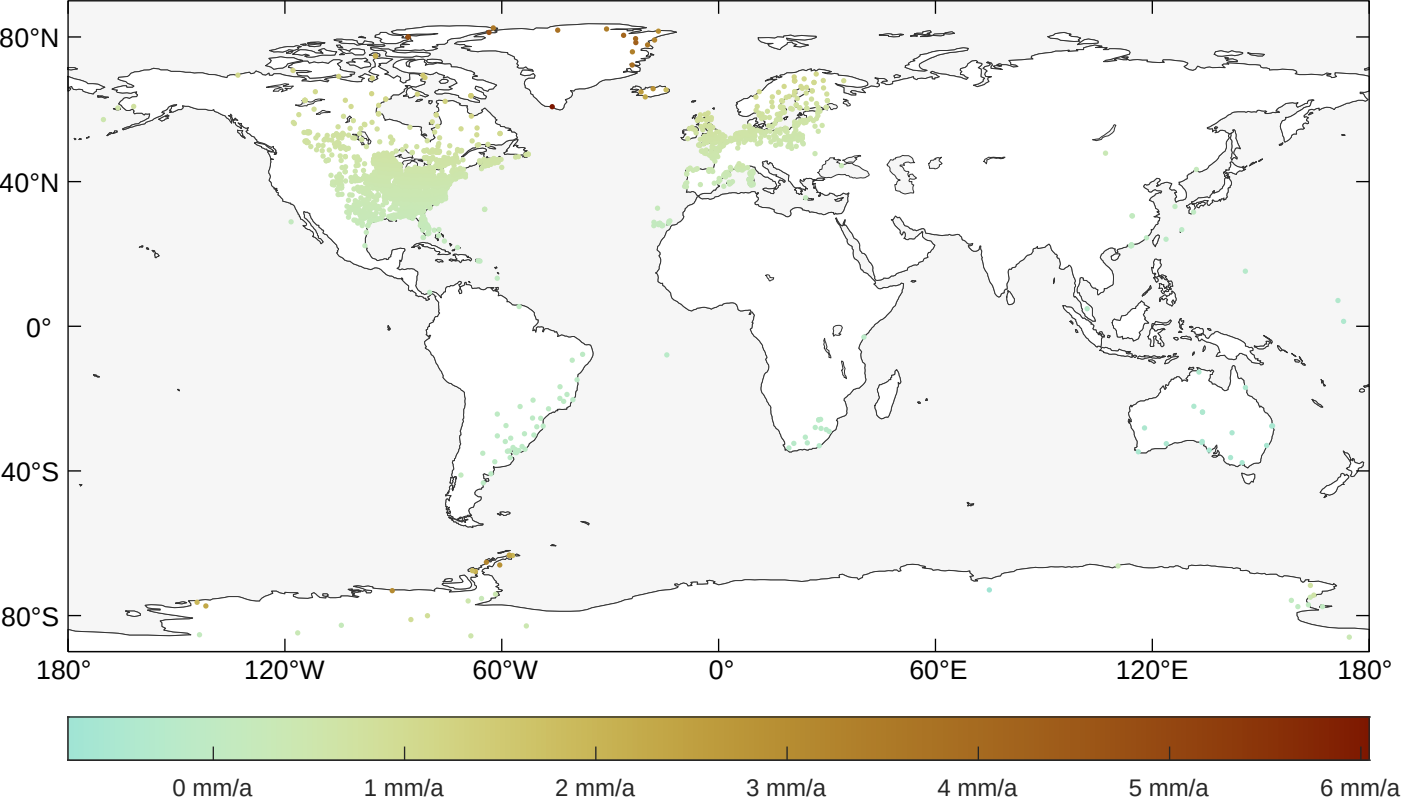
80°N
40°N
0°
40°S
80°S
180°
120°W
60°W
0°
60°E
120°E
180°
0 mm/a
1 mm/a
2 mm/a
3 mm/a
4 mm/a
5 mm/a
6 mm/a

Figure 5.

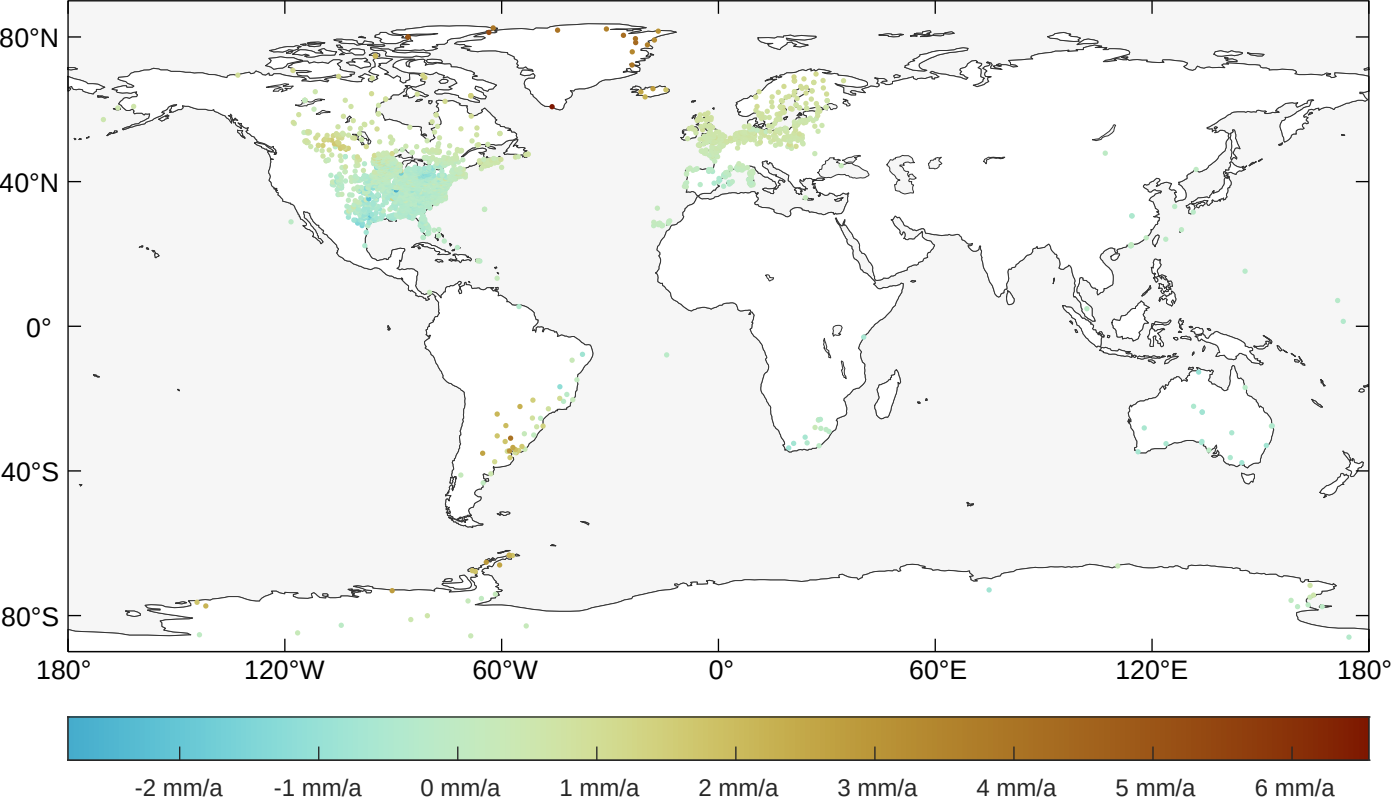
80°N
40°N
0°
40°S
80°S
180°
120°W
60°W
0°
60°E
120°E
180°
-2 mm/a
-1 mm/a
0 mm/a
1 mm/a
2 mm/a
3 mm/a
4 mm/a
5 mm/a
6 mm/a

Figure 6.

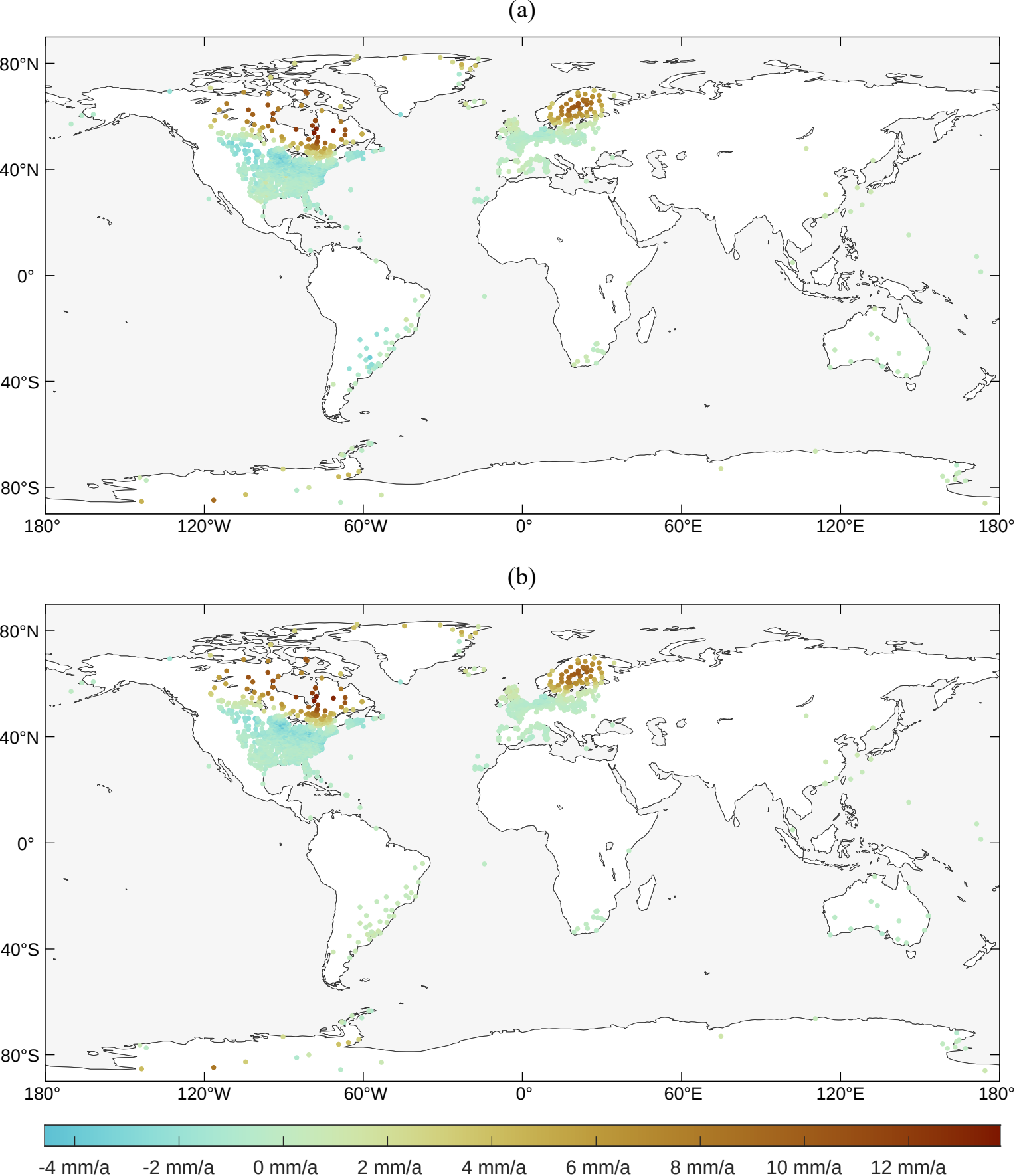
(a)
80°N
40°N
0°
40°S
80°S
180°
120°W
60°W
0°
60°E
120°E
180°
(b)
80°N
40°N
0°
40°S
80°S
180°
120°W
60°W
0°
60°E
120°E
180°
-4 mm/a
-2 mm/a
0 mm/a
2 mm/a
4 mm/a
6 mm/a
8 mm/a
10 mm/a
12 mm/a

Figure 7.

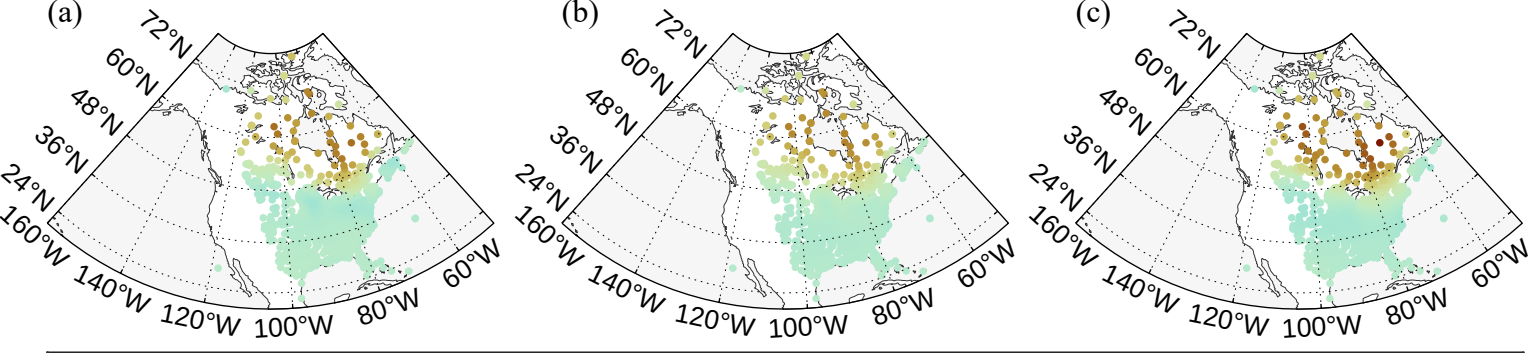
(a)
(b)
(c)
72°N
60°N
48°N
36°N
24°N
160°W
140°W
120°W
100°W
80°W
60°W
0 mm/a
5 mm/a
10 mm/a
15 mm/a
20 mm/a

Figure 7.

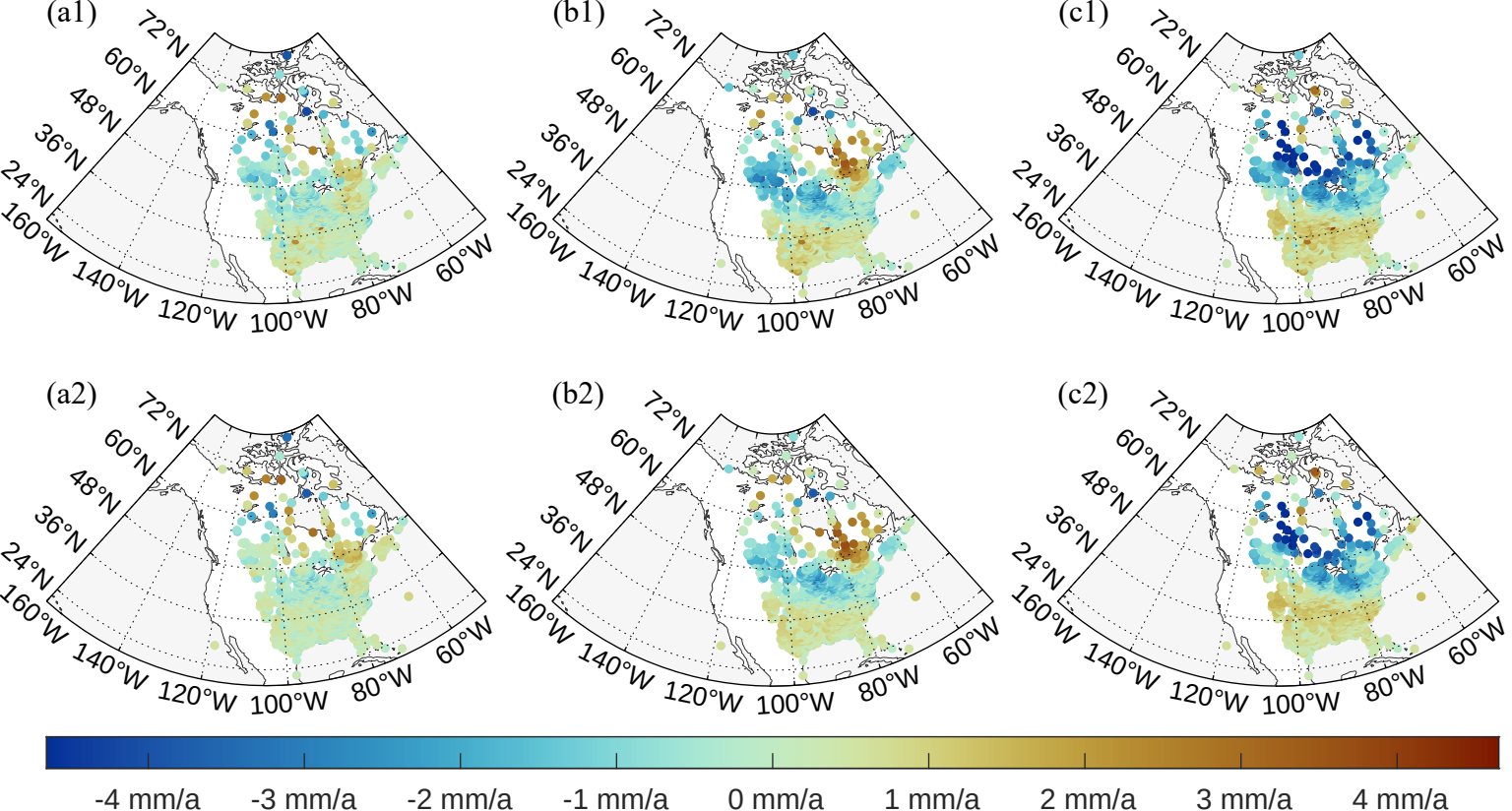
(a1)
(b1)
(c1)
(a2)
(b2)
(c2)
72°N
60°N
48°N
36°N
24°N
160°W
140°W
120°W
100°W
80°W
60°W
-4 mm/a
-3 mm/a
-2 mm/a
-1 mm/a
0 mm/a
1 mm/a
2 mm/a
3 mm/a
4 mm/a

Figure 8.

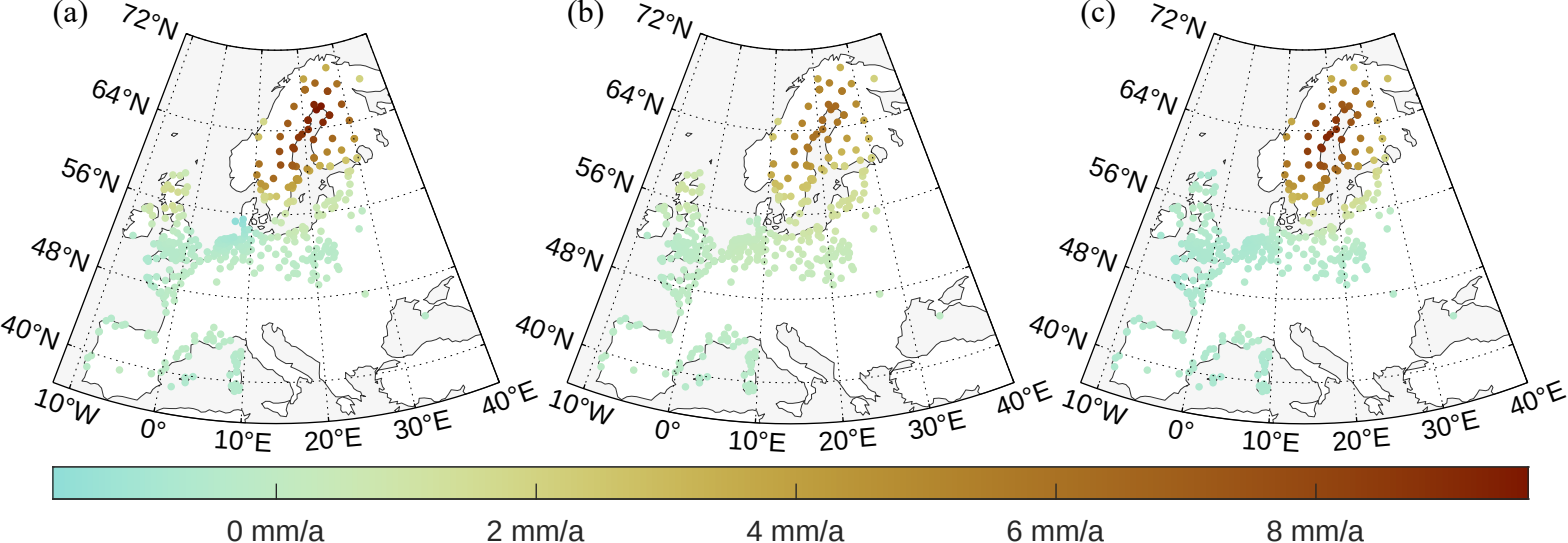
(a)
(b)
(c)
72°N
64°N
56°N
48°N
40°N
10°W
0°
10°E
20°E
30°E
40°E
0 mm/a
2 mm/a
4 mm/a
6 mm/a
8 mm/a

Figure 8.

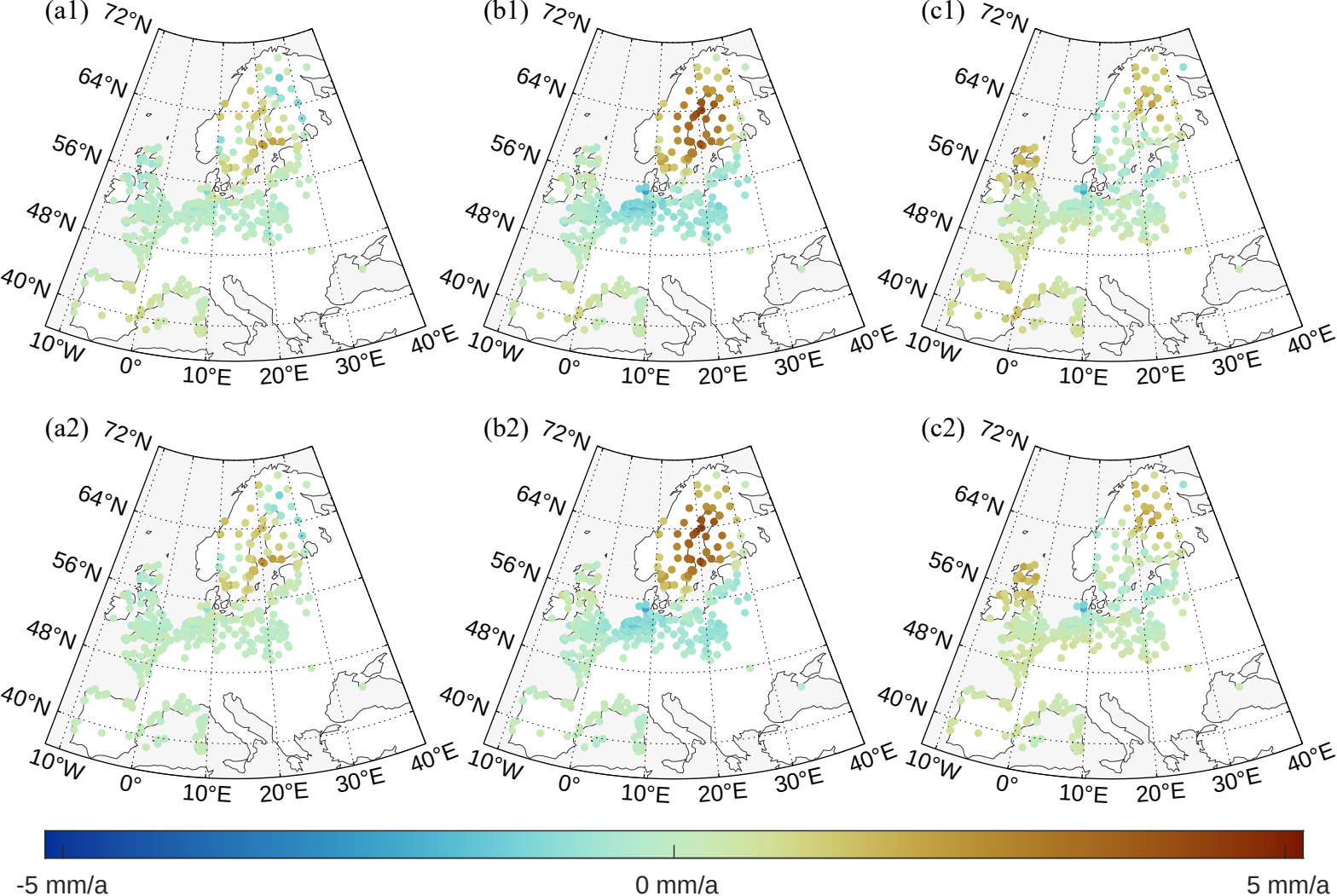
(a1)
(b1)
(c1)
(a2)
(b2)
(c2)
72°N
64°N
56°N
48°N
40°N
10°W
0°
10°E
20°E
30°E
40°E
-5 mm/a
0 mm/a
5 mm/a

Figure 9.

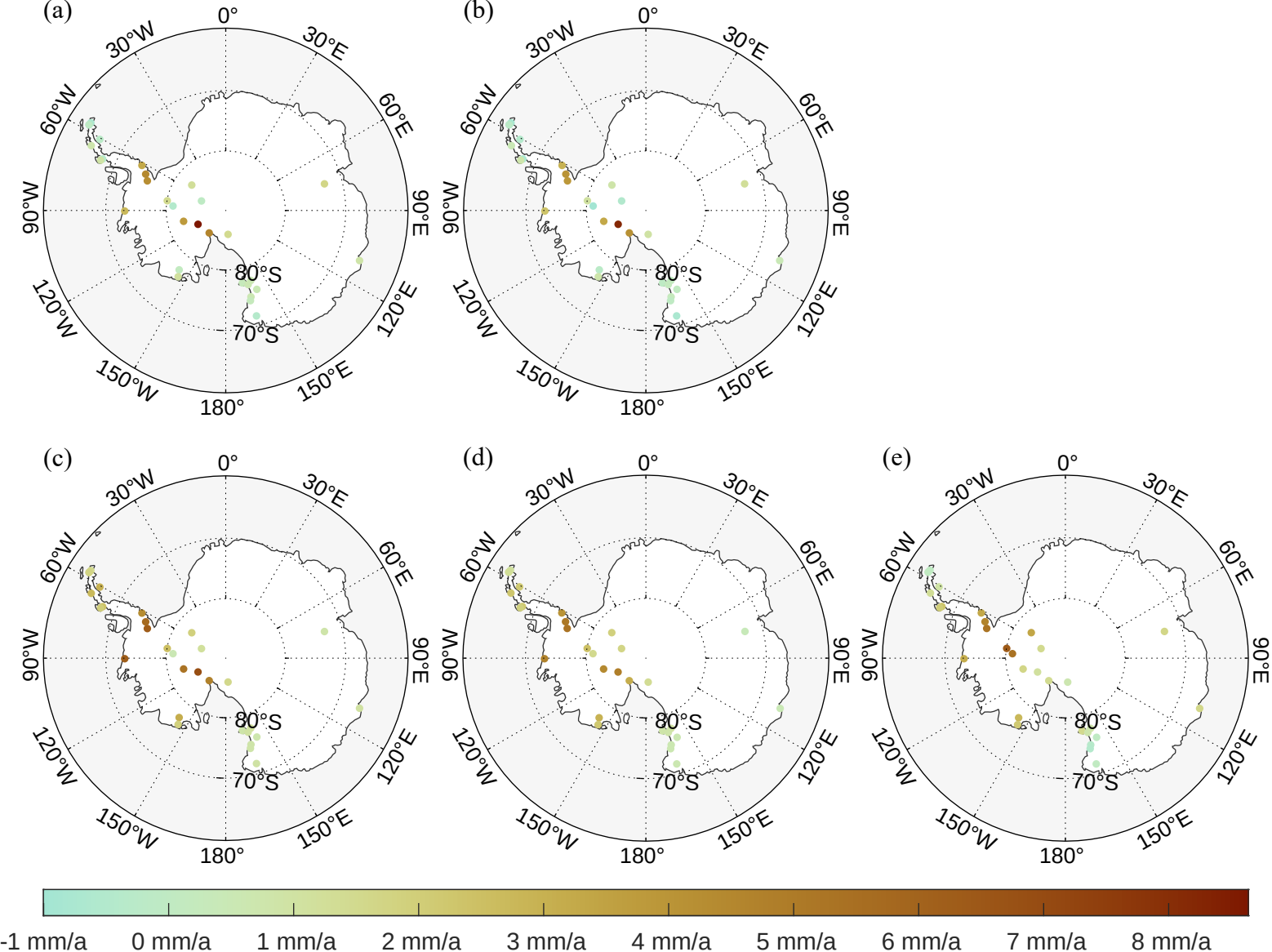
(a)
(b)
(c)
(d)
(e)
0°
30°W
30°E
60°W
60°E
90°W
90°E
120°W
120°E
150°W
150°E
180°
80°S
70°S
-1 mm/a
0 mm/a
1 mm/a
2 mm/a
3 mm/a
4 mm/a
5 mm/a
6 mm/a
7 mm/a
8 mm/a

Figure 10.

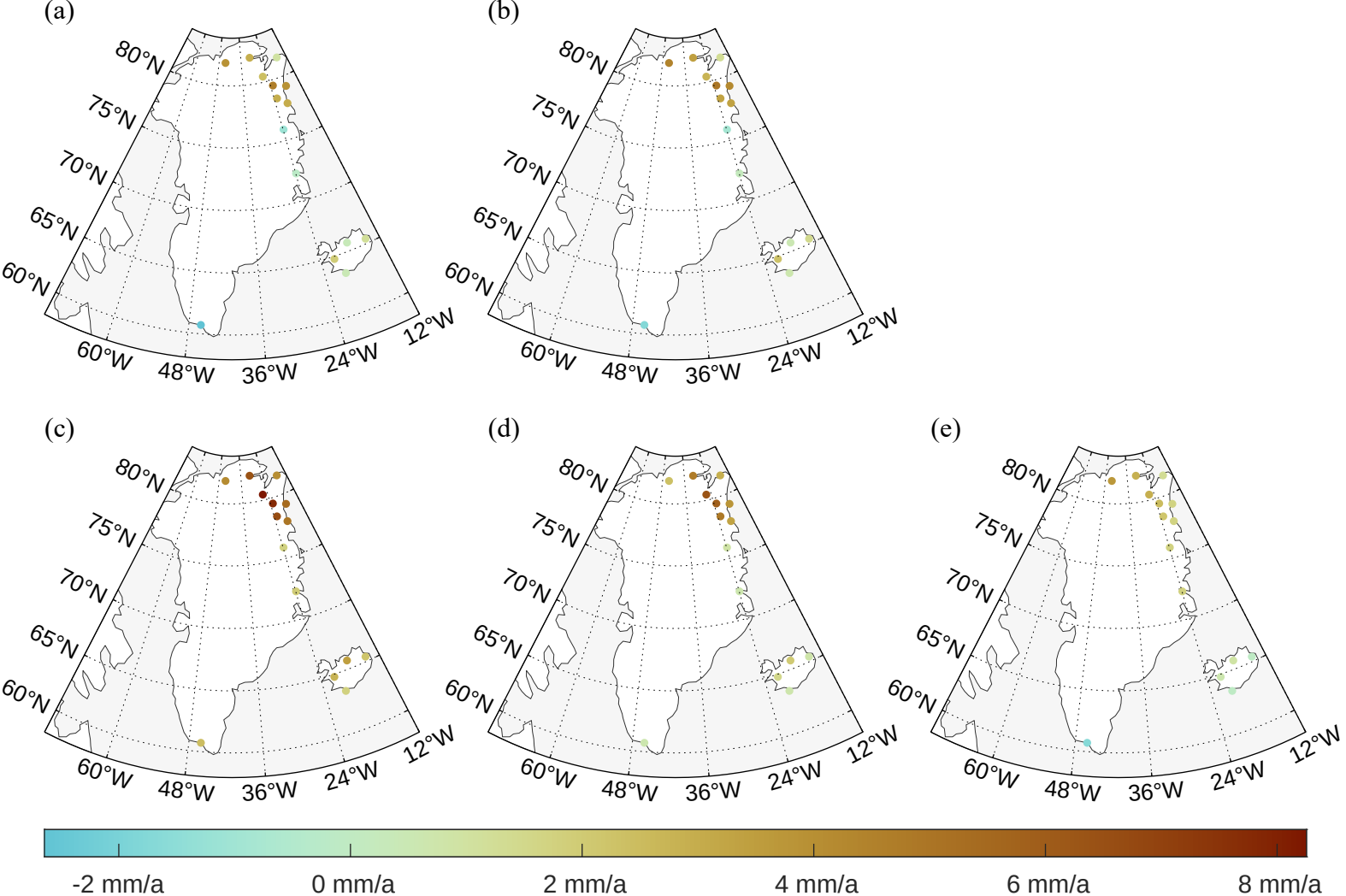
(a)
(b)
(c)
(d)
(e)
80°N
75°N
70°N
65°N
60°N
60°W
48°W
36°W
24°W
12°W
-2 mm/a
0 mm/a
2 mm/a
4 mm/a
6 mm/a
8 mm/a

Figure 11.

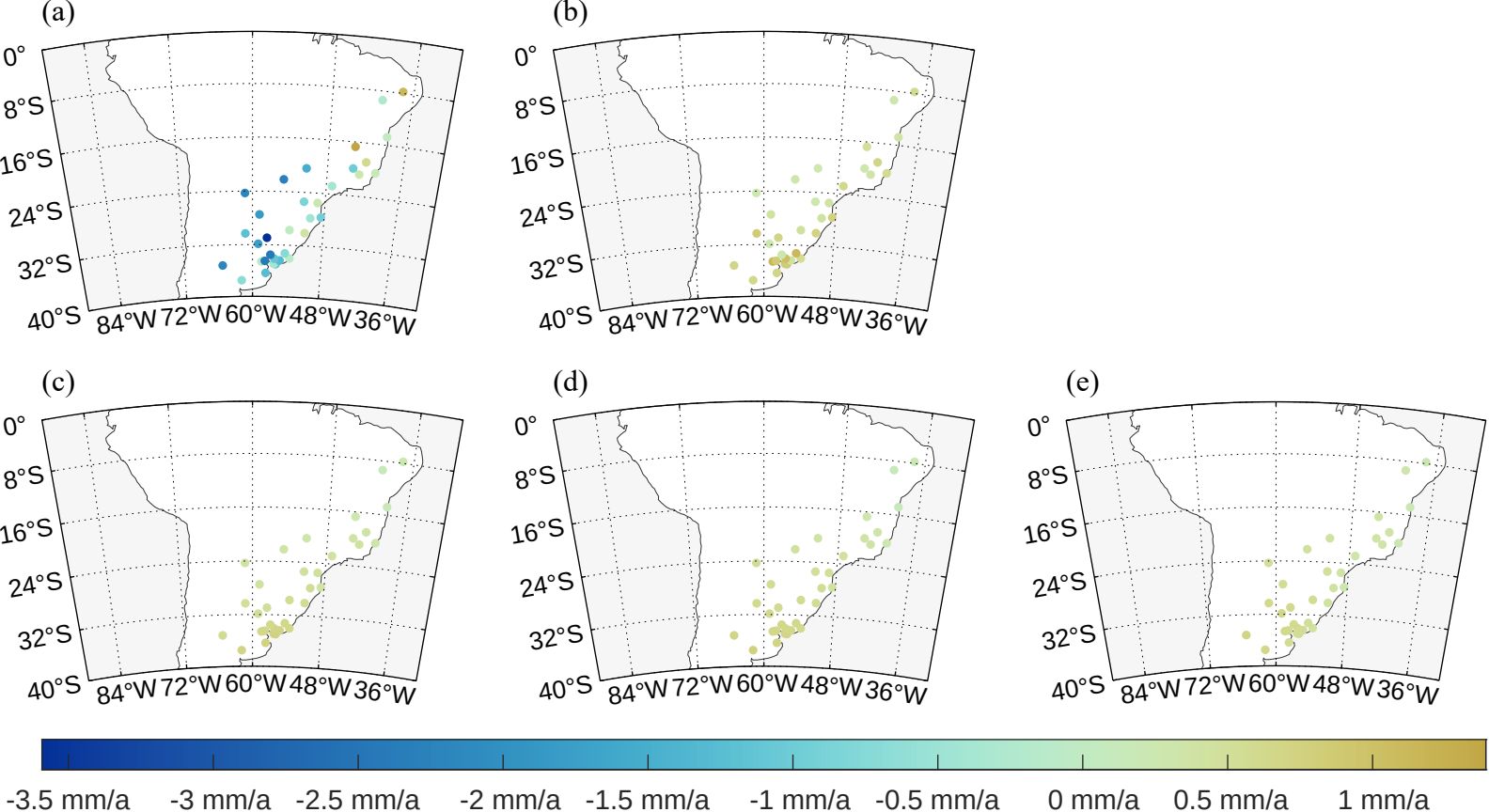
(a)
(b)
(c)
(d)
(e)
0°
8°S
16°S
24°S
32°S
40°S
84°W
72°W
60°W
48°W
36°W
-3.5 mm/a
-3 mm/a
-2.5 mm/a
-2 mm/a
-1.5 mm/a
-1 mm/a
-0.5 mm/a
0 mm/a
0.5 mm/a
1 mm/a

Figure 12.

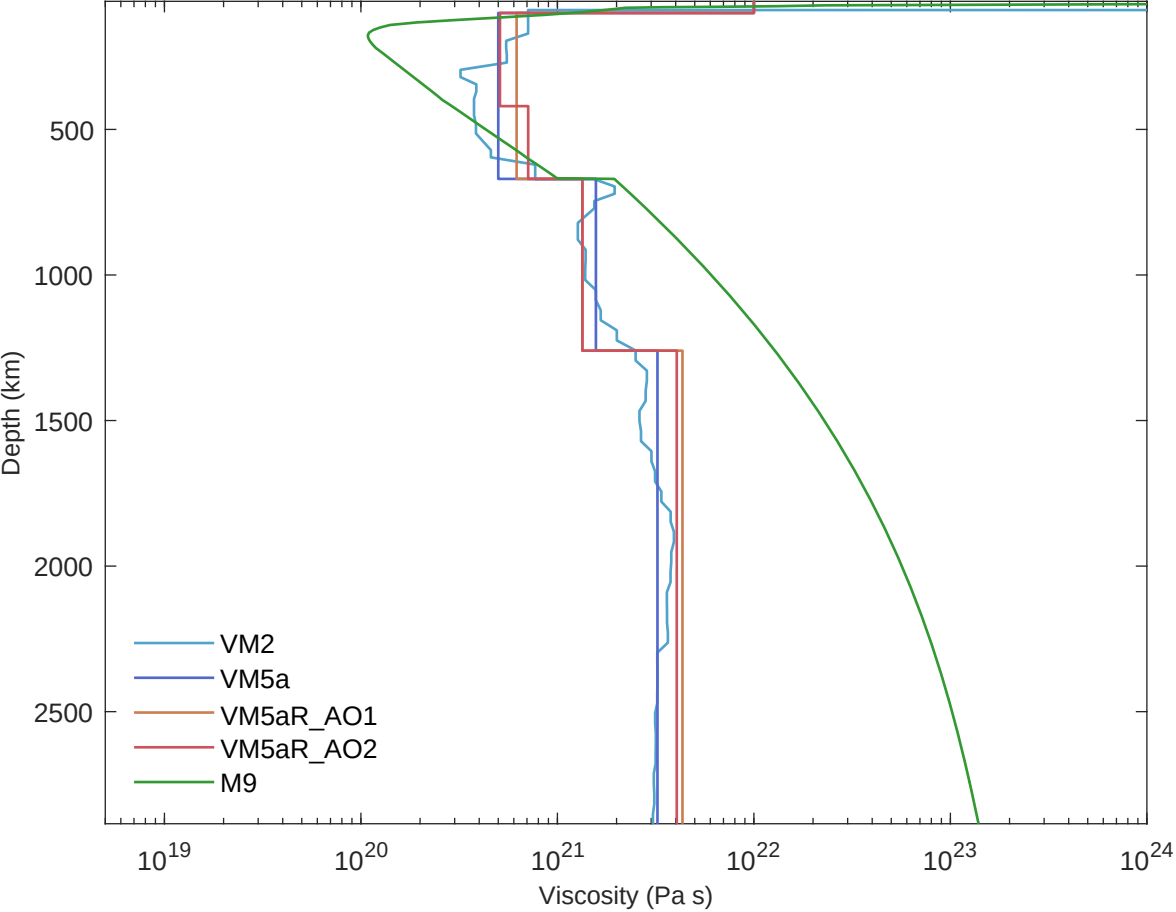
Depth (km)
500
1000
1500
2000
2500
VM2
VM5a
VM5aR_AO1
VM5aR_AO2
M9
10^{19}
10^{20}
10^{21}
10^{22}
10^{23}
10^{24}
Viscosity (Pa s)

Figure 13.

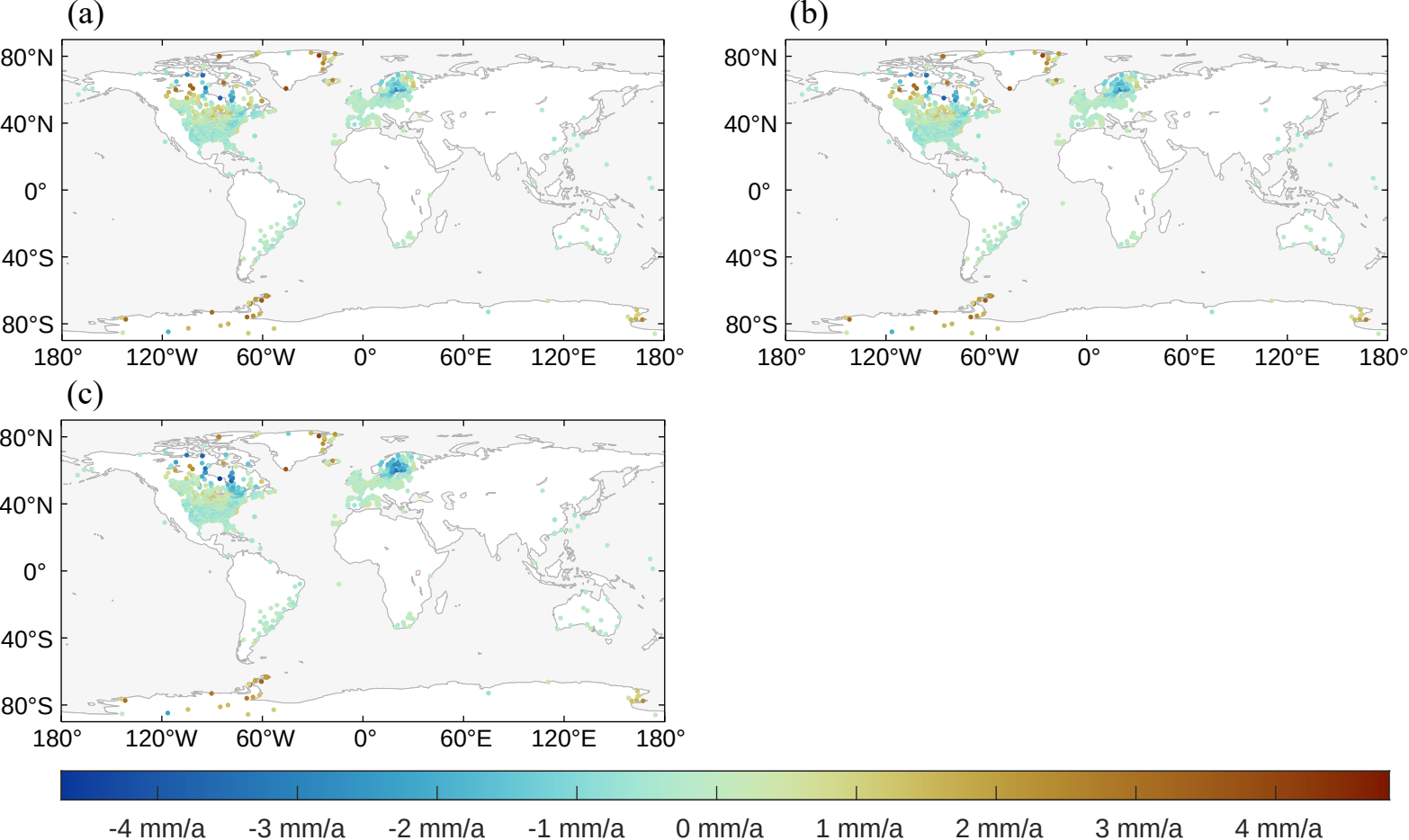
(a)
(b)
(c)
80°N
40°N
0°
40°S
80°S
180°
120°W
60°W
0°
60°E
120°E
180°
-4 mm/a
-3 mm/a
-2 mm/a
-1 mm/a
0 mm/a
1 mm/a
2 mm/a
3 mm/a
4 mm/a

Figure 14.

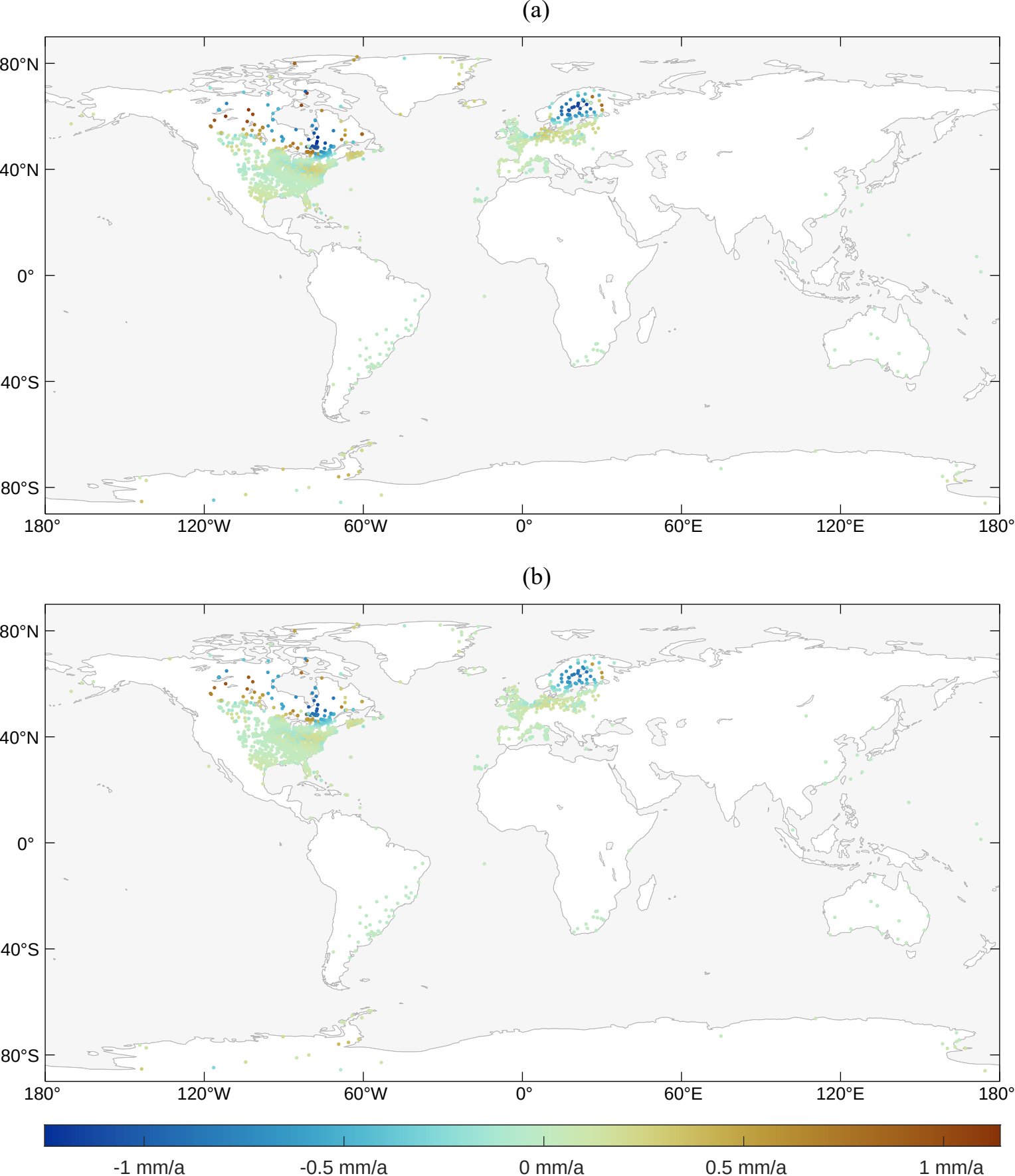
(a)
80°N
40°N
0°
40°S
80°S
180°
120°W
60°W
0°
60°E
120°E
180°
(b)
80°N
40°N
0°
40°S
80°S
180°
120°W
60°W
0°
60°E
120°E
180°
-1 mm/a
-0.5 mm/a
0 mm/a
0.5 mm/a
1 mm/a

Figure 15.

(a)

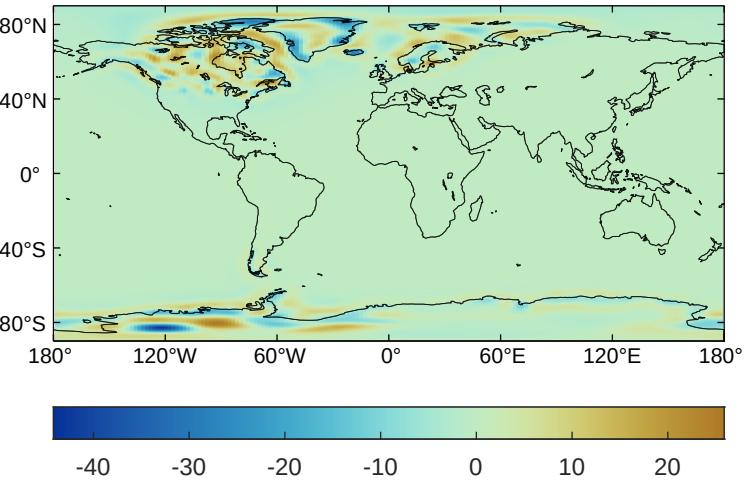
80°N
40°N
0°
40°S
80°S
180°
120°W
60°W
0°
60°E
120°E
180°
-40
-30
-20
-10
0
10
20

(b)

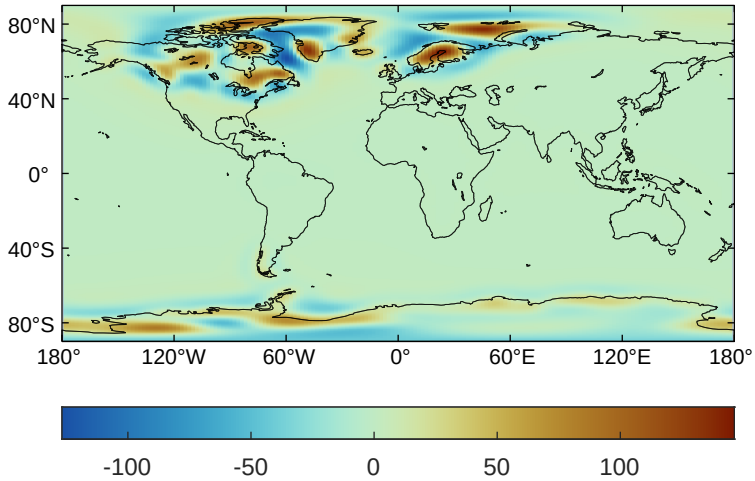
80°N
40°N
0°
40°S
80°S
180°
120°W
60°W
0°
60°E
120°E
180°
-100
-50
0
50
100

(c)

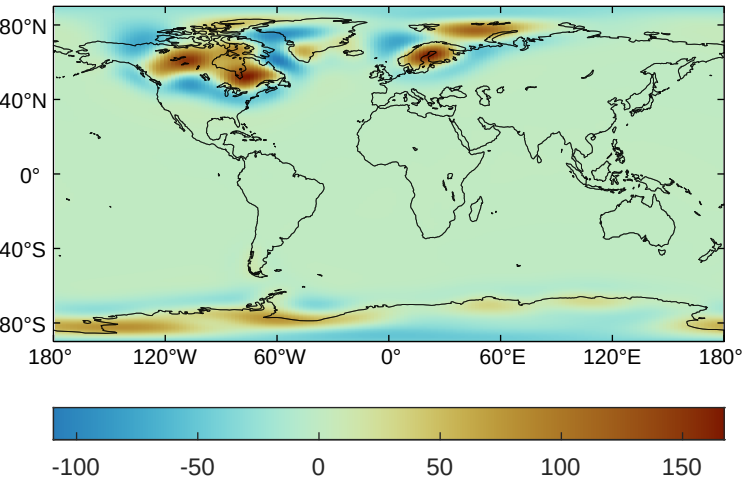
80°N
40°N
0°
40°S
80°S
180°
120°W
60°W
0°
60°E
120°E
180°
-100
-50
0
50
100
150

(d)

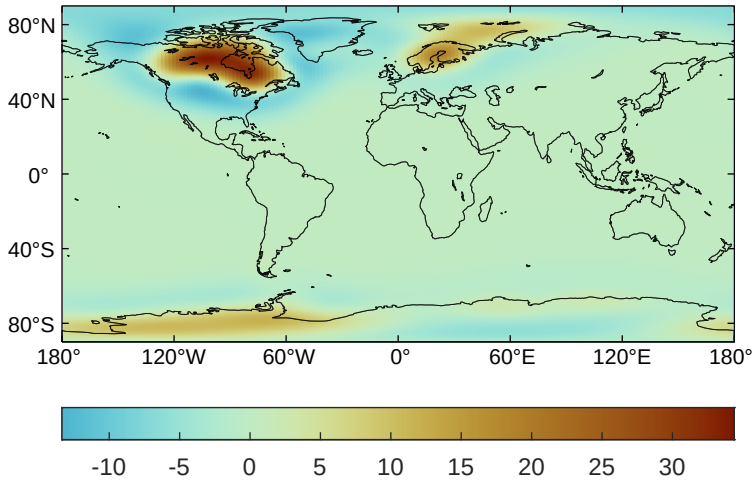
80°N
40°N
0°
40°S
80°S
180°
120°W
60°W
0°
60°E
120°E
180°
-10
-5
0
5
10
15
20
25
30

(e)

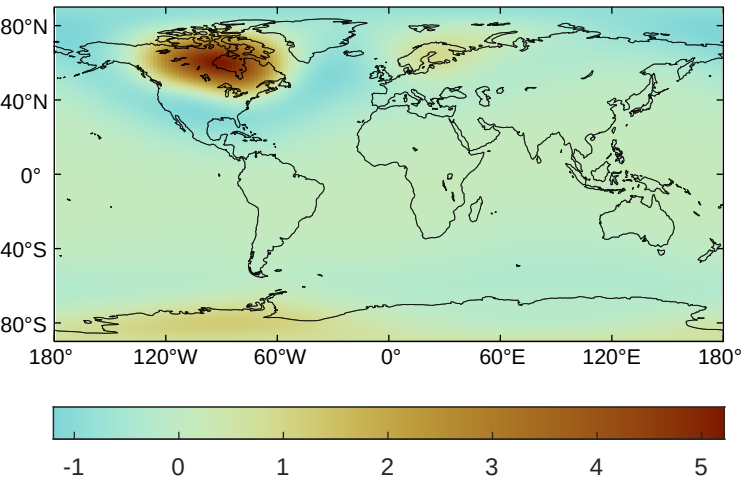
80°N
40°N
0°
40°S
80°S
180°
120°W
60°W
0°
60°E
120°E
180°
-1
0
1
2
3
4
5